Volume 9
Number 8
21 April 2025
Pages 1907–2250

Sustainable Energy & Fuels

Interdisciplinary research for the development of sustainable energy technologies

rsc.li/sustainable-energy

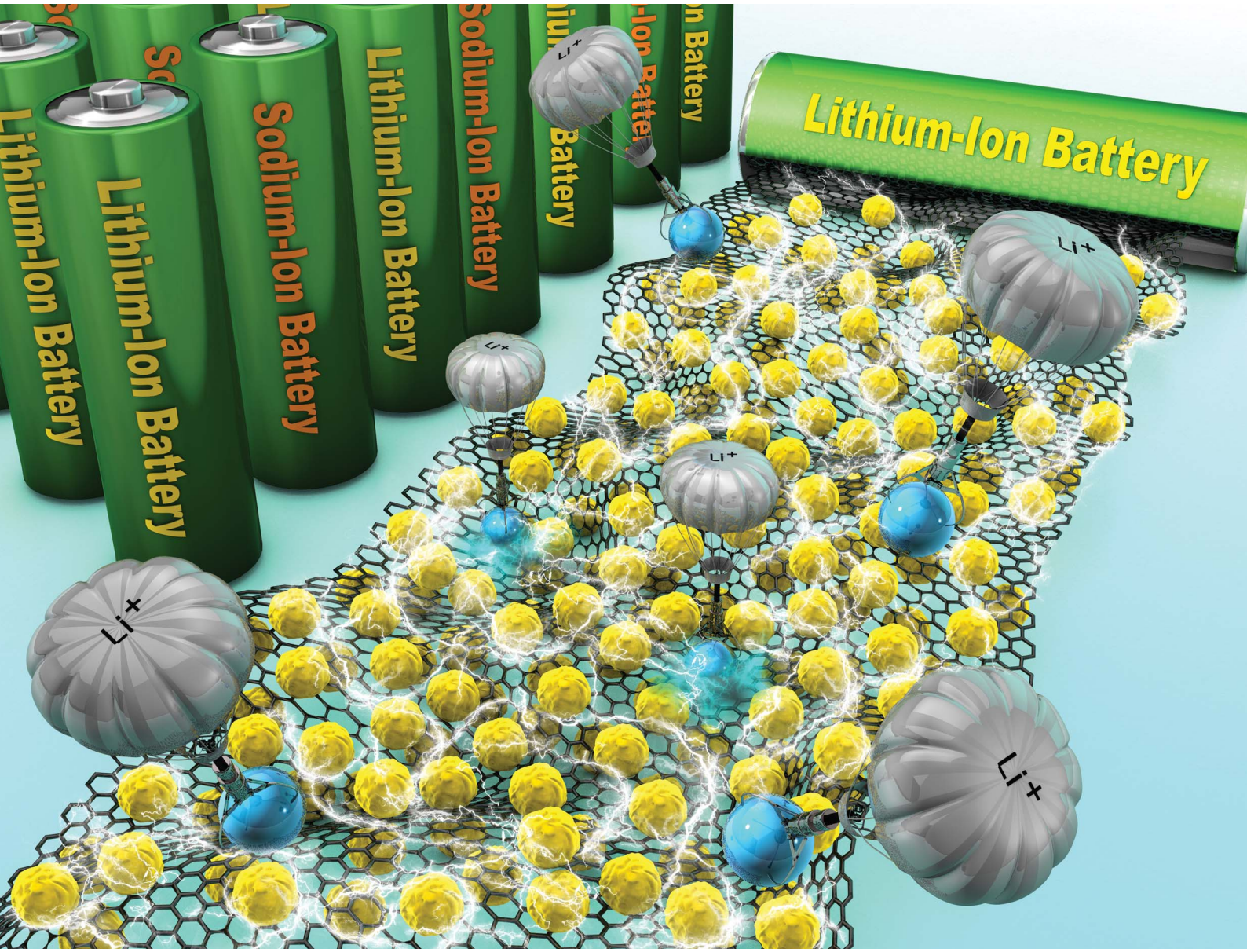

ISSN 2398-4902

ROYAL SOCIETY OF CHEMISTRY

PAPER

Seung-Min Paek *et al.*

Chemically pre-lithiated/sodiated reduced graphene oxide–antimony oxide composites for high-rate capability and long-term cycling stability in lithium and sodium-ion batteries

Sustainable Energy & Fuels

ROYAL SOCIETY OF CHEMISTRY

PAPER

View Article Online
View Journal | View Issue

Cite this: *Sustainable Energy Fuels*, 2025, **9**, 1998

Chemically pre-lithiated/sodiated reduced graphene oxide–antimony oxide composites for high-rate capability and long-term cycling stability in lithium and sodium-ion batteries†

Minseop Lee, ‡ Gi-Chan Kim‡ and Seung-Min Paek *

Utilizing ultrasonication and microwave irradiation processes, we present a straightforward synthetic route to microwave-irradiated reduced graphene oxide (MrGO)–antimony oxide (Sb_2O_3) composites used as anode materials for lithium-ion batteries (LIBs) and sodium-ion batteries (SIBs). Furthermore, after a chemical pre-lithiation (PL) and pre-sodiation (PS) process, PL-MrGO/$Li_xSb_2O_3$ and PS-MrGO/$Na_xSb_2O_3$ composites incorporating an inorganic solid electrolyte interface (SEI) layer and amorphous $Li_xSb_2O_3$/$Na_xSb_2O_3$ were prepared by drying in an ambient environment. The inorganic SEI, including Li(Na)OH already formed at the defect site where irreversible Li/Na-ion trapping occurs, inhibits the initial irreversible reaction and provides ~100% initial coulombic efficiency. In addition, the amorphous $Li_xSb_2O_3$ and $Na_xSb_2O_3$ formed before the 1st discharge process promote improved cycling stability. For LIBs, the reversible capacity of the PL-MrGO/$Li_xSb_2O_3$ anode is 877.7 mA h g^{-1} at 100 mA g^{-1} after 150 cycles and 315.3 mA h g^{-1} after 3000 cycles at 5000 mA g^{-1}. Also, for SIBs, PS-MrGO/$Na_xSb_2O_3$ exhibits a reversible capacity of 313.1 mA h g^{-1} at 1200 mA g^{-1} after 3000 cycles. This rational structural design, which considers the irreversible reactions that occur during cycling, can be extended to the development of other high-performance anode materials.

Received 5th February 2025
Accepted 19th February 2025

DOI: 10.1039/d5se00172b

rsc.li/sustainable-energy

1 Introduction

To meet the growing global demand for energy storage solutions while adhering to the principles of sustainability, researchers have increasingly focused on the development of electrochemical energy storage materials and processes.[1–6] In particular, the use of chemically pre-lithiated and pre-sodiated anode materials in lithium- and sodium-ion battery (LIB and SIB) systems has emerged as a promising approach to improve the performance and lifespan of batteries. These materials address structural stability and capacity retention issues, enhancing the batteries' overall durability and providing performance benefits throughout their lifecycle.[7–13]

The chemical pre-lithiation/sodiation process involves the incorporation of lithium or sodium ions into the anode material during synthesis. This preconditioning stabilizes the electrode structure and mitigates irreversible capacity losses that typically occur during the initial cycles of battery operation, thus substantially improving operational efficiency. Furthermore, these techniques align closely with the goals of a circular economy by reducing material waste and improving resource efficiency.

Additionally, one of the biggest challenges in current LIB and SIB research is developing anode materials that offer high energy density and long-term cycling stability.[14–19] Graphite-based anodes are widely used in LIBs due to their excellent stability and cost-effectiveness. However, the theoretical capacity of graphite is limited to 372 mA h g^{-1}, which falls short of meeting the increasing demand for high-energy-density batteries required for applications such as electric vehicles and large-scale energy storage systems.[20–23] Additionally, graphite-based anode materials in SIBs suffer from low capacity, inefficient cycling performance, and poor structural stability due to the large ionic radius of sodium ions.[24–27] In contrast, Sb-based anodes, particularly Sb_2O_3, have garnered significant attention as lithium and sodium storage materials due to their abundant resources and high theoretical capacity of 1102 mA h g^{-1}. However, like most conversion/alloy type-transition metal oxide-based electrode materials, Sb_2O_3 suffers from low electrical conductivity and significant volume changes during charge/discharge cycles, leading to physical instability and degraded cycling performance.[28–35] To address these challenges, graphene-based composites have been extensively studied. Existing literature primarily focuses on uniformly dispersing

Department of Chemistry, Kyungpook National University, Daegu 41566, Republic of Korea. E-mail: smpaek@knu.ac.kr

† Electronic supplementary information (ESI) available. See DOI: https://doi.org/10.1039/d5se00172b

‡ These authors contributed equally.

antimony oxide in a carbon matrix to mitigate volume changes and resolve conductivity issues.[36–39] Nevertheless, to address problems related to high-rate performance and long-term cycling stability, new approaches that consider the irreversible reactions occurring during the cycling process must be explored. Specifically, for the practical application of high-energy-density LIBs and SIBs, it is essential to suppress the loss of active lithium/sodium ions in the electrolyte and enhance the initial coulombic efficiency (ICE) of the anodes up to ~100%.[40–45]

This study developed a simple synthesis route for chemically pre-lithiated/sodiated MrGO/Li(Na)$_x$Sb$_2$O$_3$ composites to suppress irreversible reactions occurring during cycling.

The combined approach of introducing Li(Na)OH·Li(Na)$_2$CO$_3$ to induce an inorganic-rich solid-electrolyte interphase (SEI) and chemically pre-lithiating/sodiating Sb$_2$O$_3$ to enhance electrochemical reversibility in graphene–antimony oxide composites represents a significant advancement over conventional strategies. While traditional carbon coating or alloying techniques primarily focus on modifying the electrode surface, the approach proposed in this study effectively mitigates initial irreversible capacity loss while simultaneously improving long-term cycling performance. The formation of an inorganic-rich SEI layer stabilizes the electrode–electrolyte interface and suppresses continuous electrolyte decomposition, a common issue in conversion-type anodes. Furthermore, the pre-lithiation/sodiation process of Sb$_2$O$_3$ promotes the formation of amorphous Li$_x$Sb$_2$O$_3$, enhancing the structural stability of the electrode and ensuring excellent cycling longevity. This synergistic effect contributes to improved coulombic efficiency, reduced interfacial resistance, and increased lithium/sodium ion flux uniformity, ultimately leading to superior high-rate performance and long-term cycling stability.[46]

The PL(S)-MrGO/Li(Na)$_x$Sb$_2$O$_3$ composite was synthesized by ultrasonic and microwave treatments, followed by chemical pre-lithiation/sodiation and drying under ambient conditions. The Li(Na)OH·Li(Na)$_2$CO$_3$-based inorganic SEI introduced into the carbon domain of PL(S)-MrGO/Li(Na)$_x$Sb$_2$O$_3$ was characterized using (HR)TEM and XPS analysis. Electrochemical analyses confirmed the improved structural stability and suppression of irreversible lithium/sodium ion trapping. Additionally, it was found that the amorphous Li(Na)$_x$Sb$_2$O$_3$ formed from crystalline Sb$_2$O$_3$ minimizes irreversible reactions following the initial conversion reaction and can stably participate in lithium/sodium ion storage reactions over long-term cycling.[47–49] Notably, PL-MrGO/Li$_x$Sb$_2$O$_3$ demonstrates exceptional performance as an anode material for LIBs. The PL-MrGO/Li$_x$Sb$_2$O$_3$ anode exhibits a discharge capacity of 866.7 mA h g^{-1} at 100 mA g^{-1}, which remains at 576.9 mA h g^{-1} when the current density increases to 1000 mA g^{-1}. This value represents ~99.4% of the theoretical capacity of MrGO/Sb$_2$O$_3$ (872 mA h g^{-1}). In addition, the PL-MrGO/Li$_x$Sb$_2$O$_3$ anode retains its capacity of 877.7 mA h g^{-1} after 150 cycles at 100 mA g^{-1}. The long-term cycling stability of the PL-MrGO/Li$_x$Sb$_2$O$_3$ anode is remarkable, maintaining a capacity of 315.3 mA h g^{-1} even after 3000 cycles at a high current density of 5000 mA g^{-1}. This excellent rate performance and long-term cycling stability are also observed in SIBs. The PS-MrGO/Na$_x$Sb$_2$O$_3$ anode retains a capacity of over 78.0 mA h g^{-1} as the current density increases from 100 mA g^{-1} to 20 000 mA g^{-1}. Additionally, it retains a discharge capacity of 386.2 mA h g^{-1} after 300 cycles when the current density returns to 100 mA g^{-1}. Furthermore, in a constant current test conducted at 1200 mA g^{-1}, the PS-MrGO/Na$_x$Sb$_2$O$_3$ anode achieves a reversible capacity of 313.5 mA h g^{-1} after 3000 cycles. Consequently, this simple and rational synthesis strategy of graphene and metal oxide composites, which includes chemical pre-lithiation/sodiation, can effectively enhance long-term cycling stability and energy density.

2 Experimental

2.1. Materials

Sodium nitrate (NaNO$_3$, ≥99%), sulfuric acid (H$_2$SO$_4$, 95.0–98.0%), graphite (<20 μm), tetrahydrofuran (THF, 99%) and antimony(III) acetate (SbAc, 99.99%) were purchased from Sigma-Aldrich Corporation (USA). Potassium permanganate (KMnO$_4$, ≥99.3%), ethyl alcohol (≥94.0%) and ethylene glycol (EG, ≥99.5%) were acquired from Duksan Pure Chemical Co., Ltd (Korea). Hydrogen peroxide (H$_2$O$_2$, 34.5%) was purchased from Samchun Pure Chemical Co., Ltd (Korea). Antimony(III) oxide (Sb$_2$O$_3$, 99%) was purchased from Alpha Aesar. All reagents were used without further purification.

2.2. Synthesis of graphene oxide

Graphene oxide (GO) was synthesized using a modified Hummer's method, involving the chemical exfoliation of graphite with a strong oxidizing agent in an acidic medium.[50] Initially, graphite powder (1.0 g), sodium nitrate (NaNO$_3$, 0.75 g), and sulfuric acid (H$_2$SO$_4$, 75 mL) were mixed and stirred in an ice bath to control the exothermic reaction. Potassium permanganate (KMnO$_4$, 4.5 g) was gradually added to the mixture over the course of 1 hour, followed by stirring for two more hours in the ice bath and subsequently at room temperature for five days. The resulting GO suspension was purified by washing with H$_2$SO$_4$, hydrogen peroxide (H$_2$O$_2$), and distilled water to remove residual manganese salts and halt the oxidation process. Finally, the GO was repeatedly washed with distilled water and ethanol until a neutral pH was achieved. Then, it was collected through centrifugation at 15 000 rpm for 5 min.

2.3. Synthesis of rGO/Sb(OH)$_3$ and MrGO/Sb$_2$O$_3$

To synthesize rGO by reducing GO, antimony acetate (Sb(Ac)$_3$) and GO are reacted using ultrasonication and microwave treatments. Initially, GO and Sb(Ac)$_3$ are dissolved separately in ethylene glycol (EG) to prepare 1 g per L GO/EG and 4 g per L Sb(Ac)$_3$/EG solutions, respectively. These two solutions are then thoroughly mixed at a volume ratio of GO/EG : Sb(Ac)$_3$/EG = 25 : 65 and subjected to ultrasonic treatment for 1 hour, resulting in the formation of an rGO/Sb(OH)$_3$/EG solution. This solution is centrifuged and dried to obtain a slurry form of rGO/Sb(OH)$_3$. Finally, the obtained rGO/Sb(OH)$_3$ is subjected to microwave

treatment in a microwave oven for 10 min, yielding the final product, MrGO/Sb_2O_3.

2.4. Chemical pre-lithiation and pre-sodiation

In a glovebox filled with ultrapure Ar, 50 mg of MRGO/Sb_2O_3 powder is immersed in a 3 mL solution of 1 M lithium-biphenyl (Li-Bp) and sodium-biphenyl (Na-Bp) in THF for 1 minute and 1.2 min, respectively, followed by washing with THF. The resulting powder is vacuum-dried. The powders obtained by vacuum drying are then dried in an oven at 60 °C under an ambient atmosphere for 6 hours. The final products are named PL-MrGO/$Li_xSb_2O_3$ and PS-MrGO/$Na_xSb_2O_3$. To evaluate the effect of drying conditions on the initial coulombic efficiency (ICE) of PL-MrGO/$Li_xSb_2O_3$ electrodes, samples were dried at 60 °C for different durations (6 and 24 hours) before electrode slurry preparation and initial charge–discharge testing. The results showed that the ICE was ~99% after 6 hours of drying and remained ~97% even after 24 hours (Fig. S1†). This indicates that the 60 °C, 6-hour drying conditions were chosen for experimental convenience, and the material maintains stable electrochemical performance even after extended drying.

2.5. Calculation of theoretical capacity

The theoretical capacities of MrGO/Sb_2O_3 as an anode material were calculated based on the weight fractions of its components and their respective theoretical capacities. The weight fraction of Sb_2O_3 in MrGO/Sb_2O_3 is 35.68 wt%, and the remaining 64.32 wt% corresponds to MrGO. The theoretical capacity of Sb_2O_3 is 1102 mA h g^{-1}, while MrGO, assumed to have the same theoretical capacity as graphene, contributes 744 mA h g^{-1}. The total theoretical capacity was calculated as a weighted sum of the contributions from Sb_2O_3 and MrGO, using the following formula:

$$C_{MrGO/Sb_2O_3} = (wt_{Sb_2O_3} \times C_{Sb_2O_3}) + (wt_{MrGO} \times C_{MrGO})$$

$$C_{MrGO/Sb_2O_3} = (0.3568 \times 1102\ mA\ h\ g^{-1}) + (0.6432 \times 744\ mA\ h\ g^{-1}) = 872\ mA\ h\ g^{-1}$$

Therefore, the theoretical capacity of the MrGO/Sb_2O_3 anode is calculated to be 872 mA h g^{-1}.

2.6. Electrode preparation and Li(Na) half cells assembly

Active electrodes were fabricated by casting a slurry consisting of 70 wt% active material, 20 wt% carbon black, and 10 wt% polyacrylic acid (PAA) in *N*-methyl-2-pyrrolidone (NMP) onto copper foil. The coated electrodes were dried in a vacuum oven at 110 °C for 12 hours. These electrodes were used for evaluating the electrochemical performance of LIB and SIB anodes. CR2032 coin cells were assembled in an argon-filled glovebox (H_2O and O_2 levels < 0.1 ppm). Lithium metal was cast onto an aluminum spacer to serve as the counter electrode. A Celgard 3501 separator was used to separate the anode and counter electrode. The electrolyte consisted of a 1 M $LiPF_6$ solution in a 1 : 1 (v/v) mixture of ethylene carbonate (EC) and diethyl carbonate (DEC). Sodium metal on aluminum foil served as the counter electrode, and a Celgard 3501 separator was employed. The electrolyte comprised 1 M $NaPF_6$ in a propylene carbonate/fluoroethylene carbonate (98 : 2 w/w) solution.

Galvanostatic charge–discharge tests were performed within a voltage range of 0.01–3.0 V (*vs.* Li/Li^+) and 0.01–2.5 V (*vs.* Na/Na^+) using a battery tester (Maccor K4300). Cyclic voltammetry (CV) was conducted at scan rates of 0.1, 0.3, 0.5, and 0.8 mV s^{-1} using a potentiostat (WonATech WMPG1000). EIS measurements were performed at open-circuit potential over a frequency range of 10^{-2} to 10^5 Hz using a potentiostat (Oneartec ZIVE SP2). For DRT analysis, the MATLAB-based software 'DRTtools', available at Ciucci's GitHub repository (**https://github.com/ciuccislab/**), was utilized.[51]

2.7. Characterization

The crystalline phases of the samples were analyzed using powder X-ray diffraction (PXRD, Bruker D2 Phaser, USA) with CuKα radiation (λ = 1.54056 Å). FTIR spectra were recorded using a Nicolet iS5 FTIR spectrometer (Thermo Fisher Scientific, USA) with the KBr pellet method. Surface elemental composition and oxidation states were determined through X-ray photoelectron spectroscopy (XPS, K-Alpha, Thermo Fisher Scientific, USA). Thermogravimetric analysis (TGA) was conducted using a Discovery SDT 650 instrument (TA Instruments, USA) over a temperature range of 35–900 °C in an ambient atmosphere at a heating rate of 5 °C min^{-1}. The surface morphology of the samples was characterized *via* scanning electron microscopy (SEM, Hitachi SU8220, Japan). Transmission electron microscopy (TEM) and selected area electron diffraction (SAED) were performed using a Titan G2 Chem-iSTEM Cs Probe (FEI Company, Netherlands).

3 Results and discussion

3.1. Synthesis and chemical pre-lithiation and pre-sodiation mechanism

Fig. 1a schematically illustrates the synthesis process of PL(S)-MrGO/Li(Na)$_x$$Sb_2O_3$, while Fig. 1b shows the analysis of the crystallinity of the products using X-ray diffraction (XRD). In ethylene glycol (EG) solvent, GO nanosheets containing oxygen functional groups exhibit negative surface charges, and the positively charged $[Sb(EG)_3]^{3+}$ complexes are adsorbed through electrostatic interactions. Upon ultrasonic treatment, the temperature of the solution rises significantly due to an exothermic reaction. At elevated temperatures, the oxygen-containing species on the unstable GO nanosheet surfaces react with –OH and are removed, forming reduced graphene oxide (rGO) nanosheets. The XRD pattern of rGO/$Sb(OH)_3$ formed after ultrasonic treatment does not exhibit the peak around 8° associated with GO, nor does it show distinct crystallization peaks attributed to Sb_2O_3. However, the XRD pattern of microwave-treated MrGO/Sb_2O_3 reveals clear crystallization peaks due to the formation of Sb_2O_3 from $Sb(OH)_3$. Consequently, a simple process involving ultrasonic and microwave irradiation successfully fabricated composites containing Sb_2O_3

nanoparticles within a graphene matrix.[52] The chemical reactions occurring during the synthesis of MrGO/Sb_2O_3 are detailed in Fig. 1c. During the synthesis of MrGO/Sb_2O_3, the interaction between acetate anions and ethylene glycol in the reaction solution serves as a source of OH^-. These generated OH^- remove oxygen-containing functional groups from GO, thereby promoting the formation of rGO.

Fig. S2† presents the XRD spectra of samples where GO was dispersed in EG and then subjected to ultrasonic treatment (EG–GO) and microwave treatment (EG–MGO) in the absence of antimony acetate. These spectra confirm that no reduction of GO occurs in EG without antimony acetate, demonstrating that antimony acetate is essential for the reduction of GO during the synthesis of MrGO/Sb_2O_3. Under ambient conditions, the XRD pattern of pre-lithiated/sodiated and dried PL(S)-MrGO/Li(Na)$_x$$Sb_2O_3$ shows a decrease in peaks attributed to crystalline Sb_2O_3, indicating the formation of amorphous Li(Na)$_x$$Sb_2O_3$. The peaks observed at around 41° and 46° in the XRD spectrum of PL(S)-MrGO/Li(Na)$_x$$Sb_2O_3$ can be indexed to inorganic crystalline phases. The peaks observed around 41° and 46° can be indexed to inorganic crystalline phases. According to the PDF card (database) in Fig. S3,† the peaks near 41° and 46° are likely associated with the crystal planes of Li(Na)OH or Li(Na)$_2$$CO_3$. This suggests that during the pre-lithiation (pre-sodiation) process, reactions between Li(Na)-organic radical reagents, Sb_2O_3, and MrGO may lead to the presence of residual Li(Na)-ions, which subsequently react with moisture and oxygen in the ambient environment, resulting in the formation of Li(Na)OH and Li(Na)$_2$$CO_3$.

The chemical reactions involved in the pre-lithiation/sodiation process of MrGO/Sb_2O_3 are illustrated in Fig. 1d. When MrGO/Sb_2O_3 powder is immersed in a pre-lithiation/sodiation solution containing Li(Na)-Bp under an inert atmosphere, both MrGO and Sb_2O_3 within MrGO/Sb_2O_3 undergo a series of chemical reduction reactions. MrGO undergoes chemical reduction *via* electron transfer from biphenyl anions, with Li(Na)-ions being introduced into the disordered regions of MrGO, forming a lithiated/sodiated host. Additionally, crystalline Sb_2O_3, which has a higher redox potential than Li-Bp (0.33 V *vs.* Li^+/Li) and Na-Bp (0.12 V *vs.* Na^+/Na), transforms into amorphous Li(Na)$_x$$Sb_2O_3$.[53–61] Therefore, this straightforward pre-activation method effectively prevents the irreversible loss of lithium/sodium and mitigates the initial capacity decrease due to the amorphization of Sb_2O_3 during the early cycling process. Following the pre-lithiation/sodiation process in an inert atmosphere, excess Li(Na)-ions were removed by washing

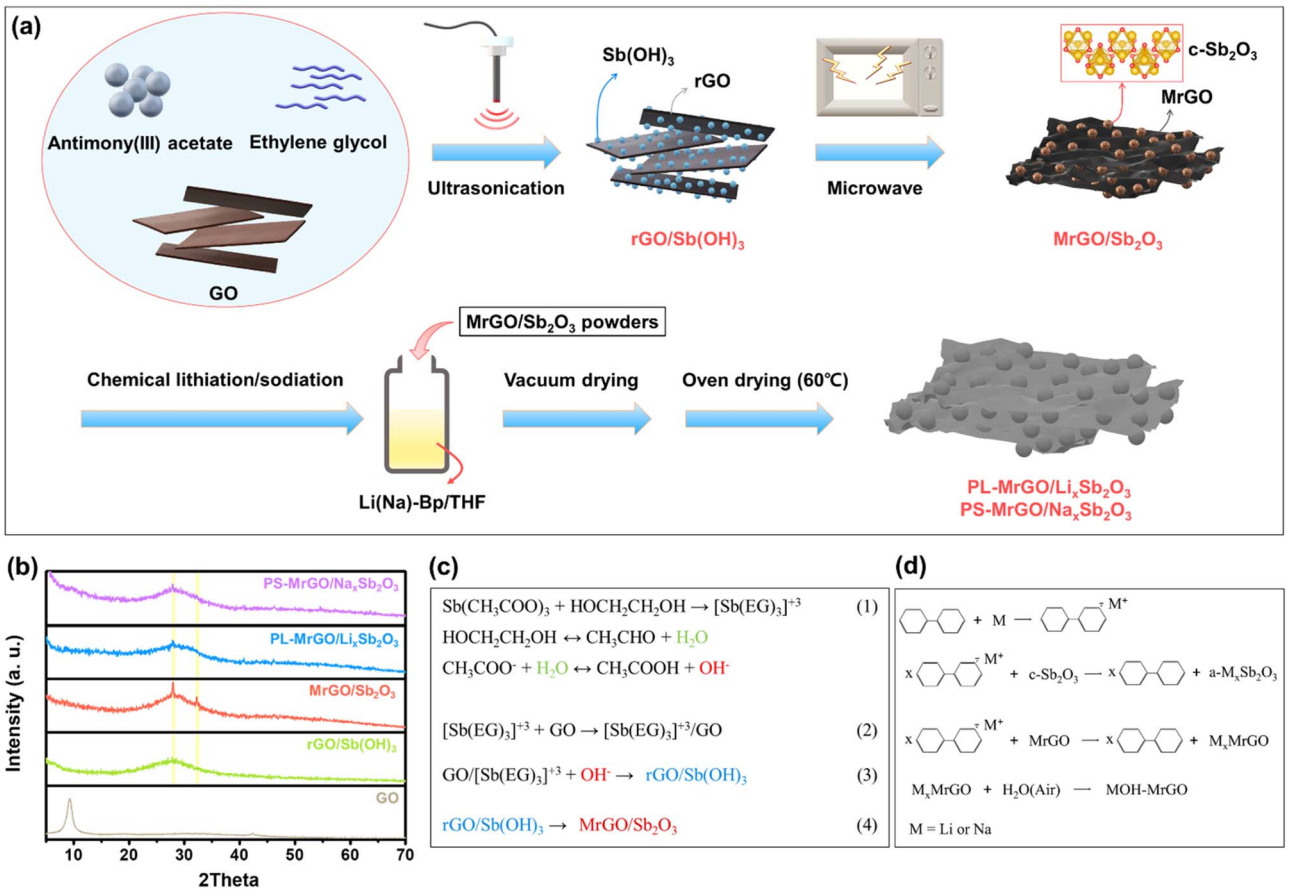

Fig. 1 (a) Schematic representation of the synthesis route for PL(S)-MrGO/Li(Na)$_x$$Sb_2O_3$ composites. (b) X-ray diffraction (XRD) patterns of GO, MrGO/Sb(OH)$_3$, MrGO/Sb_2O_3, PL-MrGO/Li$_x$$Sb_2O_3$, and PS-MrGO/Na$_x$$Sb_2O_3$. (c) Chemical reactions during the synthesis of MrGO/Sb_2O_3. (d) Chemical reactions during the pre-lithiation/sodiation process.

with THF. Subsequently, during the drying process under ambient conditions, the Li(Na)-ions introduced into the MrGO nanosheets reacted with moisture in the air to form Li(Na)OH phases. This process resulted in the integration of an inorganic SEI domain with enhanced mechanical strength and ionic conductivity into PL(S)-MrGO/Li(Na)$_x$Sb$_2$O$_3$. Furthermore, the crystalline LiOH phase incorporated into the carbon domain occupied voids where irreversible Li(Na) ion trapping could occur, thereby contributing to a high ICE.

Fig. S4† shows the Fourier Transform Infrared (FTIR) spectra of the materials utilized during the synthesis process. In the spectrum of GO, peaks corresponding to C–O, C–O–C, C=C, and C=O (carboxylic acid) confirm the presence of oxygen-containing functional groups. However, following ultrasonication treatment of antimony acetate and GO, the peaks associated with oxygen-containing groups almost disappeared or significantly diminished. After microwave irradiation, most of the oxygen-containing functional groups were removed, and only the aromatic C=C stretching mode at approximately ~1550 cm^{-1}, attributed to the MrGO nanosheets, was prominently observed.[62–67]

3.2. Thermal stability and composition analysis

To quantify the Sb_2O_3 content in MrGO/Sb_2O_3, thermogravimetric analysis (TGA) was conducted in an ambient atmosphere (Fig. S5†). The mass loss observed below 600 °C corresponds to the decomposition and combustion of carbonaceous material, with the residual mass of approximately 39.50 wt% attributed to the formation of Sb_2O_4. After the TGA scan, the XRD pattern of the residue confirmed the conversion of Sb_2O_3 to Sb_2O_4 (Fig. S6†). Based on the molar mass of Sb_2O_4, the estimated Sb_2O_3 content in MrGO/Sb_2O_3 was determined to be 37.44 wt%.[67–69] Further analysis using inductively coupled plasma (ICP) was performed to assess the Sb content in MrGO/Sb_2O_3. The Sb_2O_3 content, calculated from the molar mass of Sb obtained *via* ICP analysis, was 35.68 wt%. Additionally, X-ray photoelectron spectroscopy (XPS) elemental analysis was conducted to verify the surface composition of MrGO/Sb_2O_3, revealing an Sb_2O_3 content of 38.66 wt%. These values are consistent with the results obtained from TGA and ICP analyses, indicating that most Sb_2O_3 nanoparticles are uniformly adsorbed on the surface of the graphene nanosheets in MrGO/Sb_2O_3. A summary of the TGA, ICP, XPS, and TEM-EDS elemental analysis results for MrGO/Sb_2O_3 can be found in Table S1.†

3.3. Morphological and structural analysis

The surface morphology of the samples was characterized using scanning electron microscopy (SEM). Fig. 2a illustrates the expanded open structure of MrGO, with its increased interlayer spacing. In contrast, EG–MGO retains oxygen functional groups on the edges and basal planes of the graphene, resulting in a thicker, multilayered structure similar to GO (Fig. 2b and S7†). The SEM images of MrGO/Sb_2O_3 are distinctly different from those of EG–MGO. Fig. 2c shows that the reduced graphene nanosheets form an open structure, with a rough surface indicating the presence of Sb_2O_3 nanoparticles on the graphene nanosheets. This structure is expected to exhibit a synergistic effect, where the graphene nanosheets act as conductive channels while the Sb_2O_3 nanoparticles prevent excessive restacking of the graphene. Fig. 2d and e demonstrate the volumetric

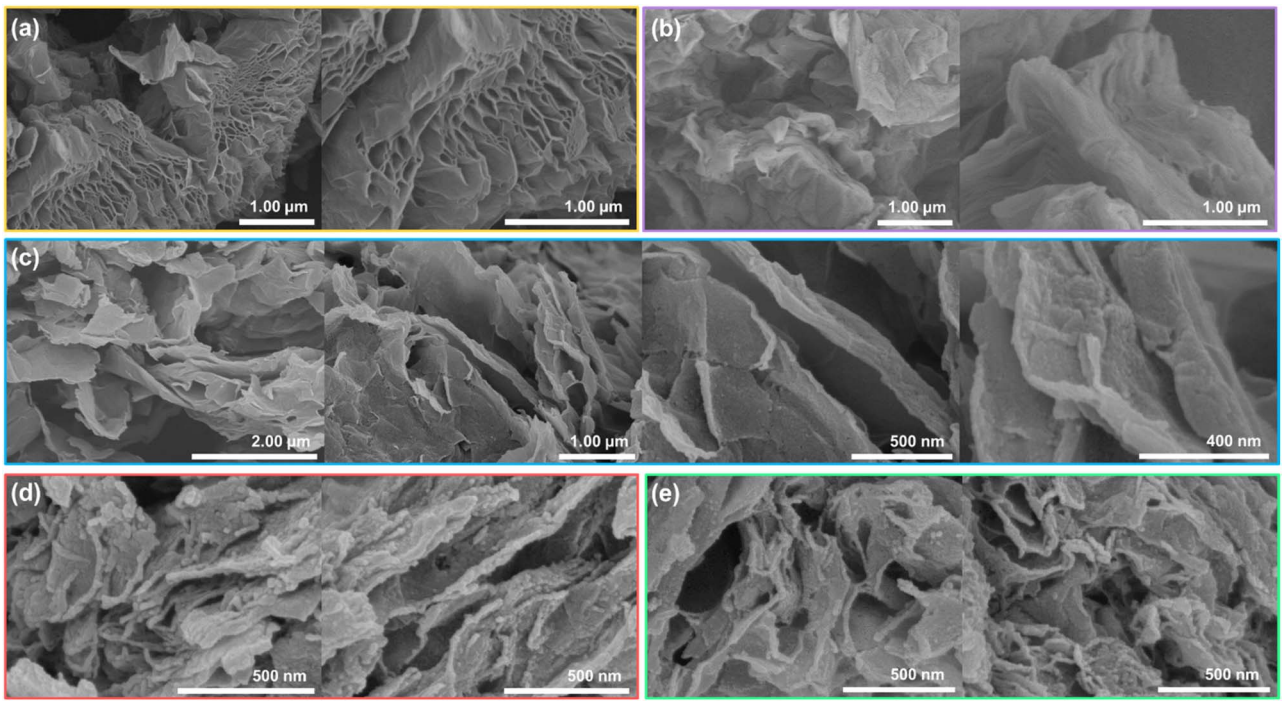

Fig. 2 (a) Field emission scanning electron microscopy (FE-SEM) images of (a) MrGO, (b) EG–MGO, (c) MrGO/Sb_2O_3, (d) PL-MrGO/$Li_xSb_2O_3$, and (e) PS-MrGO/$Na_xSb_2O_3$.

expansion due to the formation of lithiated/sodiated graphene and $Li(Na)_xSb_2O_3$ following the pre-lithiation/sodiation treatment of $MrGO/Sb_2O_3$. Therefore, utilizing the already amorphized and expanded samples as active materials through pre-lithiation/sodiation treatments is expected to enhance the physical stability of the electrodes during cycling.

The porosity of the synthesized samples was investigated using nitrogen adsorption–desorption isotherms (Fig. S8 and S9†). The specific surface area calculated by the Brunauer–Emmett–Teller (BET) method and the pore size distribution calculated by the Barrett–Joyner–Halenda (BJH) method are presented in Table S2†. The adsorption isotherms of GO and EG–MGO exhibited very low BET-specific surface areas of 26 $m^2 g^{-1}$ and 21 $m^2 g^{-1}$, respectively. In contrast, MrGO, reduced by microwave treatment under hydrated conditions, displayed a significantly higher BET-specific surface area of 240 $m^2 g^{-1}$ and increased pore volume. This suggests the presence of numerous electrochemically active sites capable of accommodating lithium/sodium ions. However, this also indicates an increase in the active surface area where irreversible reactions at the electrode/electrolyte interface may occur. Therefore, the Sb_2O_3 nanoparticles adsorbed on the surface of the graphene nanosheets and embedded within the carbon structure can help inhibit irreversible reactions on the electrode surface and within the SEI layer, thereby achieving a high ICE. The BET-specific surface areas of PL-$MrGO/Li_xSb_2O_3$ and PS-$MrGO/Na_xSb_2O_3$, which underwent pre-lithiation/sodiation treatment, were found to be 11 $m^2 g^{-1}$ and 27 $m^2 g^{-1}$, respectively. The reduction in pore volume and specific surface area can be attributed to the formation of an inorganic SEI layer containing Li(Na)OH within the pores of the carbon structure and the lithiation/sodiation of Sb_2O_3 nanoparticles.

Transmission electron microscopy (TEM) images were analyzed to gain a deeper understanding of the structural characteristics of $MrGO/Sb_2O_3$. The high-resolution (HR)TEM images in Fig. S10† clearly illustrate the wide basal spacing of MrGO nanosheets (0.39–0.41 nm) and the integration of small Sb_2O_3 nanoparticles, measuring a few nanometers, into the graphene. Additionally, Fig. S11† presents HAADF and EDS elemental mapping (C, O, and Sb) images of $MrGO/Sb_2O_3$, confirming the uniform distribution of each element. Fig. S12 and S13† show the HRTEM and EDS elemental mapping images of PL-$MrGO/Li_xSb_2O_3$ and PS-$MrGO/Na_xSb_2O_3$. After pre-lithiation/sodiation, the HRTEM and SAED images reveal the integration of amorphous nanoparticles ($Li_xSb_2O_3$ and $Na_xSb_2O_3$) into the graphene. The EDS images confirm that uniform chemical pre-lithiation/sodiation was successfully achieved through the lithium/sodium-organic composite solution.[70,71]

3.4. Chemical bonding and surface chemistry analysis

Fig. 3 and S14a–e† show the X-ray photoelectron spectroscopy (XPS) spectra of $MrGO/Sb_2O_3$, PL-$MrGO/Li_xSb_2O_3$, and PS-$MrGO/Na_xSb_2O_3$ electrodes. The XPS elemental analysis results of PL-$MrGO/Li_xSb_2O_3$ and PS-$MrGO/Na_xSb_2O_3$ are detailed in Tables S3 and S4.† In Fig. 3a, the C 1s spectra of $MrGO/Sb_2O_3$ show a significantly lower relative intensity of oxygen-containing functional groups compared to GO synthesized *via* the Hummer's method (Fig. S15†). This indicates that the GO nanosheets were effectively reduced during the synthesis of $MrGO/Sb_2O_3$. Additionally, the presence of an additional peak at 285.4 eV in the C 1s spectra of $MrGO/Sb_2O_3$ can be attributed to the C–O(–Sb) bond, suggesting the formation of strong electronic interactions between Sb_2O_3 and the MrGO nanosheets.[72] In Fig. 3b, the Sb 3d spectra of $MrGO/Sb_2O_3$ overlap with the O 1s spectra. The signals at 530.7 eV and 540.1 eV correspond to Sb^{3+} $3d_{3/2}$ and Sb^{3+} $3d_{5/2}$ in c-Sb_2O_3, respectively.[73–76] The O 1s spectral signal at 531.9 eV arises from lattice oxygen and oxygen-containing functional groups on the

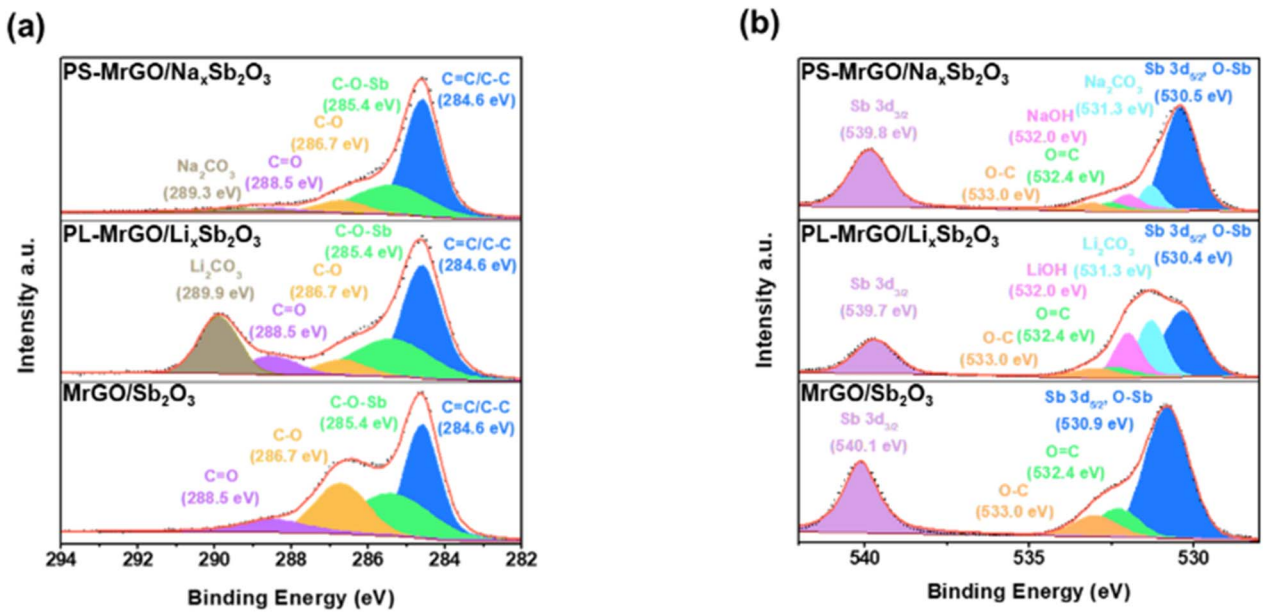

Fig. 3 High-resolution XPS spectra of (a) C 1s and (b) Sb 3d & O 1s for $MrGO/Sb_2O_3$, PL-$MrGO/Li_xSb_2O_3$, and PS-$MrGO/Na_xSb_2O_3$.

graphene surface. After pre-lithiation, the C 1s spectra of PL-MrGO/$Li_xSb_2O_3$ reveal an additional peak attributed to Li_2CO_3, while the Sb 3d and O 1s spectra exhibit new peaks assigned to LiOH (Fig. 3c and d). These findings suggest that Li^+-ions react with atmospheric moisture to form LiOH, which subsequently reacts with CO_2 in air to form Li_2CO_3 (Fig. S14d†). Furthermore, the formation of amorphous $Li_xSb_2O_3$ shifts the Sb $3d_{3/2}$ and Sb $3d_{5/2}$ peaks to lower binding energies (530.4 eV and 539.7 eV, respectively).[77–81] In the C 1s spectra of PS-MrGO/$Na_xSb_2O_3$ presented in Fig. 3e, an additional peak corresponding to Na_2CO_3 is observed. The Sb 3d, O 1s, and Na 1s spectra confirm the formation of Na_2CO_3 and NaOH (Fig. 3f and S14e†). Furthermore, the formation of amorphous $Li_xSb_2O_3$ shifts the Sb $3d_{3/2}$ and Sb $3d_{5/2}$ peaks to lower binding energies (530.4 eV and 539.7 eV, respectively).[82–84] The Li(Na)OH·$Li(Na)_2CO_3$ formed on the electrode surface after pre-lithiation/sodiation plays a crucial role in guiding inorganic-rich SEI growth during charge/discharge cycles. Typically, Sb_2O_3-based electrodes undergo significant volume changes during cycling, leading to continuous SEI destruction and reformation. This process often results in the formation of a thick organic-rich SEI layer and accumulation of insoluble byproducts from electrolyte decomposition. Such effects increase interfacial resistance and deteriorate long-term electrochemical stability. However, the inorganic-rich SEI layer exhibits high mechanical strength and effectively mitigates excessive SEI growth. This property helps suppress unnecessary electrolyte consumption, thereby reducing initial irreversible capacity loss and enhancing the long-term cycling stability of the electrode.[46]

3.5. Lithium storage performance of PL-MrGO/$Li_xSb_2O_3$

To understand the effects of pre-lithiation and the structural synergy of composites, the electrochemical performance of PL-MrGO/$Li_xSb_2O_3$ was compared with that of MrGO/Sb_2O_3, MrGO and bare Sb_2O_3. The rate performance of each electrode was evaluated at current densities ranging from 100 to 1000 mA g^{-1} (Fig. 4a). The comparison of charge/discharge capacities and capacity retention rates over the initial 35 cycles for PL-MrGO/$Li_xSb_2O_3$, MrGO/Sb_2O_3, Sb_2O_3, and MrGO electrodes presented in Fig. 4a is shown in Fig. S16.† The PL-MrGO/$Li_xSb_2O_3$ electrode exhibited reversible capacities of 866.7 mA h g^{-1} (2nd cycles), 716.3 mA h g^{-1} (10th cycles), 656.7 mA h g^{-1} (15th cycles), 611.6 mA h g^{-1} (20th cycles), 580.8 mA h g^{-1} (25th cycles), and 573.7 mA h g^{-1} (30th cycles) at current densities of 100, 300, 500, 700, 900, and 1000 mA g^{-1}, respectively. The capacity retention rates relative to the 2nd cycle were 82.6%, 75.8%, 70.6%, 67.0%, and 66.2%, respectively. The MrGO/Sb_2O_3 electrode, under the same conditions, showed capacities of 850.8 mA h g^{-1} (2nd cycles), 678.8 mA h g^{-1} (10th cycles), 615.8 mA h g^{-1} (15th cycles), 573.2 mA h g^{-1} (20th cycles), 541.5 mA h g^{-1} (25th cycles), and 518.2 mA h g^{-1} (30th cycles), with retention rates of 79.8%, 72.4%, 67.4%, 63.6%, and 60.9%, respectively.

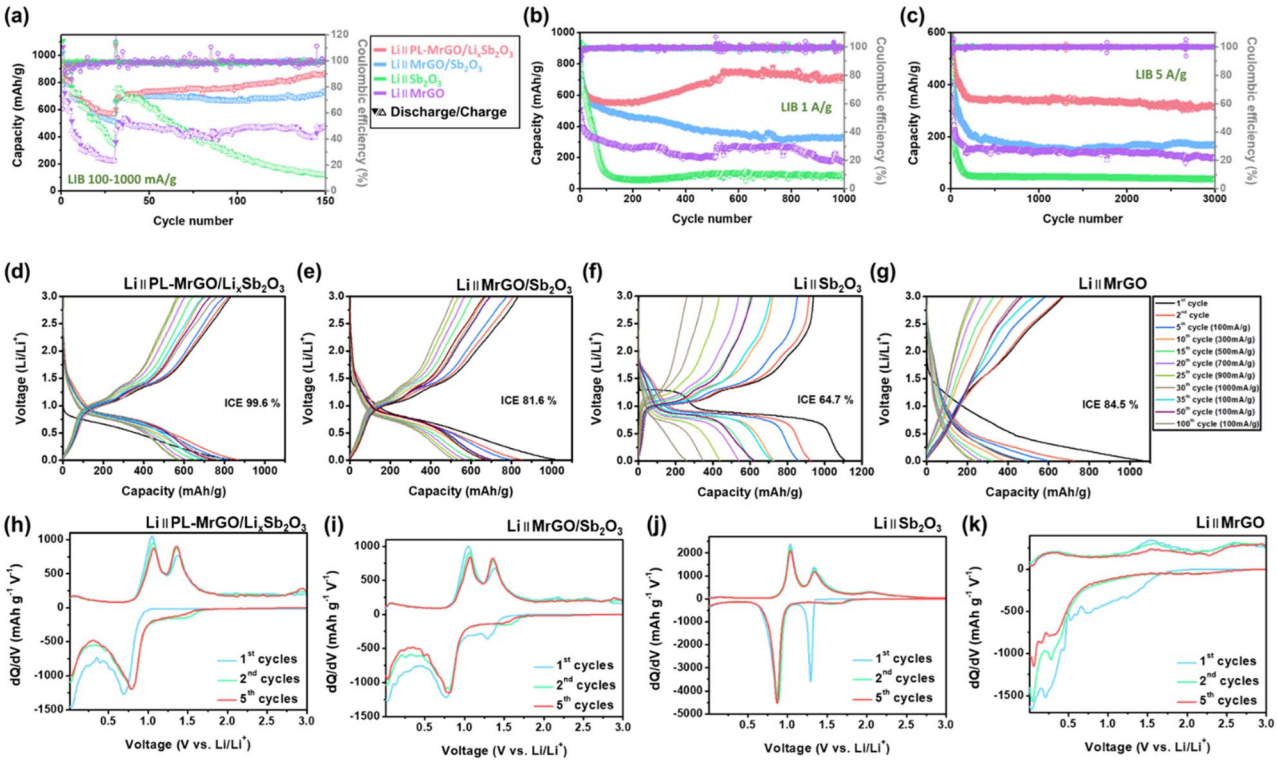

Fig. 4 Lithium storage performance: (a) rate performance of the PL-MrGO/$Li_xSb_2O_3$, MrGO/Sb_2O_3, bare Sb_2O_3 and MrGO electrodes measured at different current densities (100–1000 mA g^{-1}). Long-term cycling performance at (b) 1000 mA g^{-1} and (c) 5000 mA g^{-1}. Charge–discharge profiles of (d) PL-MrGO/$Li_xSb_2O_3$, (e) MrGO/Sb_2O_3, (f) bare Sb_2O_3 and (g) MrGO electrodes at different current densities (100–1000 mA g^{-1}). dQ/dV curves of (h) PL-MrGO/$Li_xSb_2O_3$, (i) MrGO/Sb_2O_3, (j) bare Sb_2O_3 and (k) MrGO electrodes.

At 100 mA g^{-1}, the initial discharge/charge capacities and ICE values for the PL-MrGO/$Li_xSb_2O_3$ and MrGO/Sb_2O_3 electrodes were 834.0/830.8 mA h g^{-1} (ICE = 99.6%) and 1020.4/832.2 mA h g^{-1} (ICE = 81.6%), respectively. The MrGO/Sb_2O_3 electrode exhibited a lower ICE due to irreversible SEI formation, Li-ion trapping at graphene defect sites, and irreversible reactions between Sb_2O_3 and lithium ions during the initial discharge. On the other hand, the PL-MrGO/$Li_xSb_2O_3$ electrode suppressed this irreversible reaction by forming amorphous $Li_xSb_2O_3$ and lithiated MrGO after the pre-lithiation process, achieving a high ICE. Furthermore, after reverting the current density to 100 mA g^{-1}, the PL-MrGO/$Li_xSb_2O_3$ and MrGO/Sb_2O_3 electrodes retained discharge capacities of 877.7 and 736.4 mA h g^{-1}, respectively, at the 150th cycle, with capacity retention rates of 101.3% and 86.6%. These results are especially important compared to previously reported Sb-based anodes, as summarized in Table S5,† which provides a comprehensive comparison of various synthesis strategies and their corresponding electrochemical lithium storage performance. Compared to conventional Sb-based electrodes, PL-MrGO/$Li_xSb_2O_3$ exhibits superior rate capability and long-term cycling stability. These advantages demonstrate that the chemical pre-lithiation strategy and inorganic SEI formation provide a more effective solution to the critical problems of Sb-based anodes.

In long-term cycling tests conducted at 1000 mA g^{-1}, the PL-MrGO/$Li_xSb_2O_3$ and MrGO/Sb_2O_3 electrodes exhibited capacities of 715.7 and 333.5 mA h g^{-1}, respectively, after 1000 cycles (Fig. 4b). Additionally, in cycling tests performed at 5000 mA g^{-1}, the PL-MrGO/$Li_xSb_2O_3$ and MrGO/Sb_2O_3 electrodes retained capacities of 315.3 and 169.4 mA h g^{-1}, respectively, after 3000 cycles (Fig. 4c). These results emphasize the superior cycling performance of the PL-MrGO/$Li_xSb_2O_3$ electrode compared to MrGO, bare Sb_2O_3, and MrGO/Sb_2O_3 electrodes.

The superior long-term cycling performance of the PL-MrGO/$Li_xSb_2O_3$ electrode can be attributed to the formation of an initial SEI layer during the chemical pre-lithiation/sodiation process, which acts as a stable, protective barrier at the electrode–electrolyte interface. Typically, Sb_2O_3-based electrodes undergo significant volume changes during charge/discharge cycles, leading to continuous SEI cracking and reformation. This process results in the formation of an irregular SEI structure, continuous electrolyte consumption, and an increase in interfacial electronic and ionic resistance, ultimately compromising long-term electrochemical stability. In contrast, the PL-MrGO/$Li_xSb_2O_3$ electrode synthesized in this study forms an inorganic-rich SEI layer composed of $Li(Na)OH \cdot Li(Na)_2CO_3$, which provides high mechanical strength and effectively suppresses excessive SEI growth and degradation. As a result, the stability of the SEI layer and the reduction in interfacial resistance ensure that lithium-ion diffusion within the electrode remains efficient throughout extended cycling. Consequently, the PL-MrGO/$Li_xSb_2O_3$ electrode retains a high reversible capacity even after prolonged charge/discharge cycles, demonstrating its excellent long-term cycling stability.

Fig. 4d–g present the charge–discharge profiles of PL-MrGO/$Li_xSb_2O_3$, MrGO/Sb_2O_3, MrGO, and bare Sb_2O_3 electrodes, corresponding to Fig. 4a. The bare Sb_2O_3 electrode exhibits a distinct plateau at ~0.9 V, whereas the PL-MrGO/$Li_xSb_2O_3$ and MrGO/Sb_2O_3 electrodes show more linear profiles, indicating more pseudocapacitive behaviour over the test voltage range of 0.01–3.0 V. Furthermore, the average charge potentials for each electrode are shown in Fig. S17.† The PL-MrGO/$Li_xSb_2O_3$ and MrGO/Sb_2O_3 electrodes, which incorporate a graphene matrix, exhibit a minimal polarization increase even as the current density increases from 100 to 1000 mA g^{-1}, demonstrating the formation of highly conductive graphene–Sb_2O_3 composites. In contrast, the bare Sb_2O_3 electrode shows larger polarization and a significant increase in operating potential (~0.2 V) with increasing current density along with poor capacity retention, highlighting its inferior electrical conductivity properties (Fig. S17†). Fig. 4h–k present the dQ/dV curves derived from the charge–discharge profiles. The MrGO/Sb_2O_3 and Sb_2O_3 electrodes exhibit a prominent irreversible lithiation peak at ~1.3 V during the 1st cycle, attributed to the irreversible conversion reaction of Sb_2O_3. However, the PL-MrGO/$Li_xSb_2O_3$ electrode, having undergone pre-lithiation, already forms an amorphous $Li_xSb_2O_3$ phase, thereby avoiding such irreversible reactions in the 1st cycle.

The Ragone plots in Fig. S18† illustrate the energy density (W h kg^{-1}) and power density (W kg^{-1}) calculated based on the mass of active material for PL-MrGO/$Li_xSb_2O_3$ and MrGO/Sb_2O_3 electrodes in LIBs. The PL-MrGO/$Li_xSb_2O_3$ electrode consistently delivers a high energy density across various power density conditions. This observation suggests that the pre-lithiation process significantly enhances the electrode's reversible energy storage capacity and efficiency.

Several factors contribute to the superior performance of the PL-MrGO/$Li_xSb_2O_3$ electrode. Firstly, the pre-lithiation process improves the structural stability of the electrode material, thereby reducing structural damage during repeated charge/discharge cycles. Secondly, the combination of MrGO and Sb_2O_3 optimizes electron transport pathways and enhances conductivity, thereby maximizing the electrochemical performance of the electrode. Specifically, amorphous $Li_xSb_2O_3$ exhibits high energy density, while graphene nanosheets offer excellent conductivity and a large surface area, resulting in a synergistic effect between these two materials.

3.6. Lithium storage kinetics and reaction mechanism

Fig. 5a–d show the cyclic voltammetry (CV) curves for PL-MrGO/$Li_xSb_2O_3$, MrGO/Sb_2O_3, bare Sb_2O_3, and MrGO electrodes over the initial 15 cycles measured at a scan rate of 0.1 mV s^{-1} within the voltage range of 0.01–3.0 V. In the first cycle, the CV curve for the MrGO/Sb_2O_3 electrode exhibits two reduction peaks. The peak at 1.15 V corresponds to the partially reversible conversion reaction of Sb_2O_3 to Sb and the formation of Li_2O, while the peak at 0.7 V is attributed to the alloying reaction of Sb and the formation of the SEI.[85–87] However, for the PL-MrGO/$Li_xSb_2O_3$ electrode, the reduction peak at 0.7 V associated with the alloying reaction is observed, while the peak corresponding to the partially reversible conversion reaction of Sb_2O_3 is absent. This absence is due to the pre-lithiation process, which results in the formation of amorphous $Li_xSb_2O_3$. Additionally, the

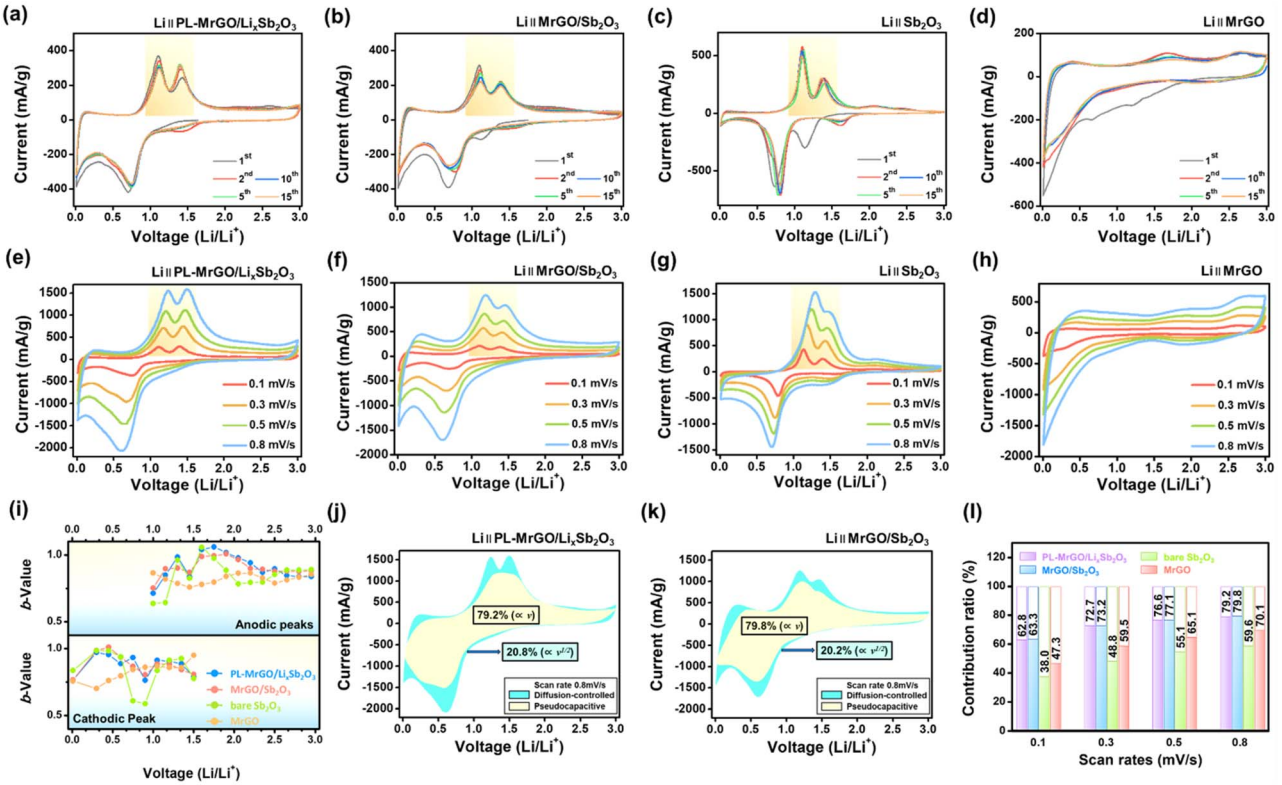

Fig. 5 Lithium storage kinetics analysis: cyclic voltammetry (CV) curves of (a) PL-MrGO/$Li_xSb_2O_3$, (b) MrGO/Sb_2O_3, (c) bare Sb_2O_3 and (d) MrGO electrodes at a scan rate of 0.1 mV s^{-1}. CV curves of (e) PL-MrGO/$Li_xSb_2O_3$, (f) MrGO/Sb_2O_3, (g) bare Sb_2O_3 and (h) MrGO electrodes at various scan rates (0.1–0.8 mV s^{-1}). (i) Comparison of *b*-values at different voltages (0.01–3.0 V). Separation of the pseudocapacitive and diffusion-controlled charge storage processes at the (j) PL-MrGO/$Li_xSb_2O_3$ and (k) MrGO/Sb_2O_3 electrodes. (l) Comparison of the pseudocapacitive contributions.

sharp peak around 0.01 V is attributed to the insertion of lithium ions into graphene. The oxidation peaks at 1.18 V for both MrGO/Sb_2O_3 and PL-MrGO/$Li_xSb_2O_3$ electrodes result from the alloying and de-alloying reactions between Sb and Li, while the peak at 1.48 V is due to the re-oxidation of Sb to Sb_2O_3. The redox reactions during the first cycle for the MrGO/Sb_2O_3 electrode can be summarized as follows:[47]

$$Sb_2O_3 + 6Li^+ + 6e^- \rightarrow 2Sb + 3Li_2O \text{ (partially reversible due to the formation of } Li_2O)$$

$$Sb + xLi^+ + xe^- \rightarrow Li_xSb\ (x \leq 3, \text{reversible})$$

In subsequent cycles, the redox peak pairs corresponding to the conversion and alloying reactions are consistently observed at 1.53/1.48 V and 0.73/1.18 V, indicating the reversible nature of these processes in Sb_2O_3 nanoparticles. Notably, the oxidation peak at 1.48 V for the PL-MrGO/$Li_xSb_2O_3$ electrode is stronger than those for the MrGO/Sb_2O_3 and bare Sb_2O_3 electrodes, indicating a higher degree of reversibility in the conversion/alloying reaction. Furthermore, the CV curves for subsequent cycles overlap well after the 1st cycle, demonstrating the reversible lithium-ion storage behaviour of the electrode. Fig. 5e–h present the CV curves of PL-MrGO/$Li_xSb_2O_3$, MrGO/Sb_2O_3, MrGO, and bare Sb_2O_3 electrodes measured at various scan rates ranging from 0.1 to 0.8 mV s^{-1}. The relationship between the peak current (i) and the scan rate (v, mV s^{-1}) is used to calculate the *b*-value (eqn (1) and (2)).

$$i = av^b \quad (1)$$

$$\log i = b \log v + \log a \quad (2)$$

A *b*-value close to 0.5 indicates that the diffusion-controlled process dominates the lithium-ion storage behaviour, while a *b*-value close to 1.0 suggests surface charge storage behaviour.[88–90]

Therefore, the *b*-values calculated for the reduction and oxidation processes of PL-MrGO/$Li_xSb_2O_3$ and MrGO/Sb_2O_3 electrodes show that both electrodes exhibit surface charge storage behaviour (Fig. 5i). Integrating the MrGO framework with small Sb_2O_3 nanoparticles provides rapid electron transport and efficient lithium-ion pathways, enhancing the diffusion-independent pseudocapacitive behaviour. Therefore, the capacitive-controlled and diffusion-controlled currents were calculated using eqn (3) and (4) to analyze the capacitive contribution quantitatively.

$$i(V) = k_1 v + k_2 v^{\frac{1}{2}} \quad (3)$$

$$\frac{i(V)}{v^{1/2}} = k_1 v^{1/2} + k_2 \quad (4)$$

The terms $k_1 v$ and $k_2 v^{\frac{1}{2}}$ represent the capacitive and diffusion-controlled currents, respectively, allowing the quantification of the capacitive current from the CV curve at specific potentials (Fig. 5j and k).[88–91] Fig. 5l compares the capacitive contributions of PL-MrGO/$Li_xSb_2O_3$, MrGO/Sb_2O_3, MrGO, and bare Sb_2O_3 electrodes at various scan rates. The PL-MrGO/$Li_xSb_2O_3$ and MrGO/Sb_2O_3 electrodes exhibit the highest capacitive-controlled ratios, reaching 79.2% and 79.8% at 0.8 mV s^{-1}, respectively. Therefore, the excellent cycling stability and rate performance of the PL-MrGO/$Li_xSb_2O_3$ and MrGO/Sb_2O_3 electrodes can be attributed to the diffusion-independent pseudo-capacitive behaviour. However, since the capacitive contributions of the PL-MrGO/$Li_xSb_2O_3$ and MrGO/Sb_2O_3 electrodes show minimal differences, further EIS analysis was conducted to explain the performance enhancement before and after pre-lithiation.

Fig. 6a–c and S19† show the Nyquist plots of PL-MrGO/Li_x-Sb_2O_3, MrGO/Sb_2O_3, MrGO, and bare Sb_2O_3 electrodes measured at various charge/discharge states. All electrodes exhibit a decreasing trend in charge transfer resistance up to the 100th cycle. Fig. 6d–f present the distribution of relaxation times (DRT) plots for a more detailed comparison of the internal resistance changes for each electrode. The MrGO electrode showed the highest increase in resistance due to SEI formation in the high-frequency region after the 1st cycle.[92–95] In contrast, the resistance increase due to SEI formation in the PL-MrGO/$Li_xSb_2O_3$ electrode was negligible. Furthermore, the PL-MrGO/$Li_xSb_2O_3$ electrode exhibited lower internal resistance over prolonged cycling compared to MrGO/Sb_2O_3, indicating its superior electrical conductivity.

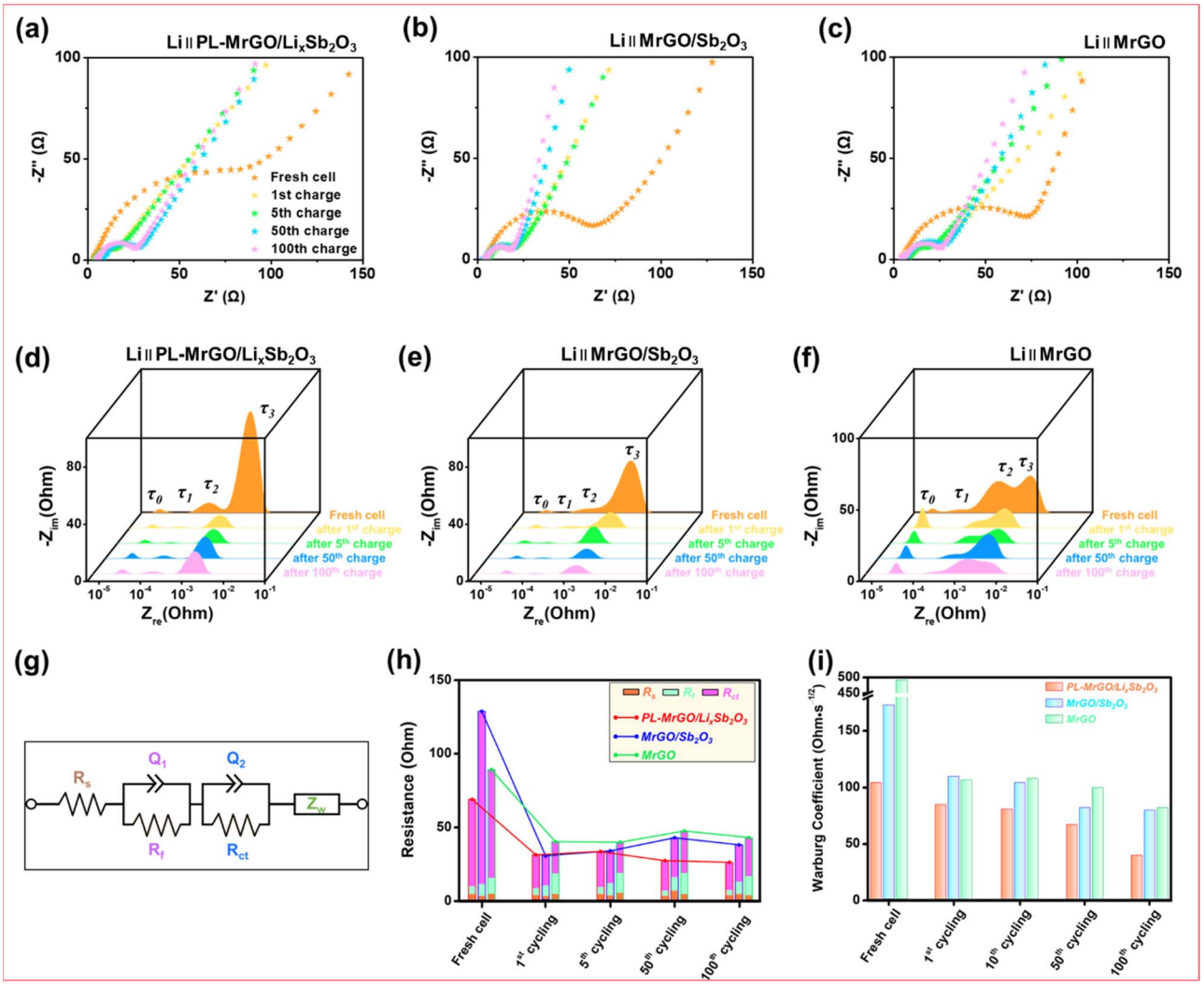

Fig. 6 Electrochemical impedance spectroscopy analysis in LIBs: Nyquist plot of the (a) PL-MrGO/$Li_xSb_2O_3$, (b) MrGO/Sb_2O_3 and (c) MrGO electrodes measured up to the 100th cycle. Distribution of relaxation times (DRT) plot of the (d) PL-MrGO/$Li_xSb_2O_3$, (e) MrGO/Sb_2O_3 and (f) MrGO electrodes. (g) Equivalent circuit model (ECM) for fitting EIS data (the impedance parameters are provided in Table S6†). (h) Comparison of the parameters from the ECM fits and (i) Warburg coefficients.

Using the Equivalent Circuit Model (ECM) presented in Fig. 6g, the impedance components of each electrode were separated and analyzed (Table S6†). The ECM fitting results for the PL-MrGO/$Li_xSb_2O_3$ electrode exhibit low charge-transfer resistance and SEI resistance, which are associated with the stable interfacial structure formed through chemical pre-lithiation (Fig. 6h). In contrast, the fitting results for the MrGO/Sb_2O_3 electrode indicate higher resistance values, reflecting the instability of the electrode–electrolyte interface. Additionally, the comparison of Warburg coefficients in Fig. 6i reveals that the PL-MrGO/$Li_xSb_2O_3$ electrode retains a low Warburg coefficient even after extended cycling, indicating efficient lithium-ion diffusion within the MrGO matrix.[96–99] Conversely, the bare Sb_2O_3 electrode shows a sharp increase in the Warburg coefficient, signifying performance degradation related to ion diffusion (Fig. S19†). As a result, the PL-MrGO/$Li_xSb_2O_3$ electrode demonstrates excellent electrochemical performance and long-term stability, attributed to the stabilization of the SEI layer and improved conductivity.

3.7. Sodium storage performance of PS-MrGO/$Na_xSb_2O_3$

Fig. 7a–c illustrate the performance of PS-MrGO/$Na_xSb_2O_3$, MrGO/Sb_2O_3, bare Sb_2O_3, and MrGO electrodes in SIBs. The PS-MrGO/$Na_xSb_2O_3$ electrode demonstrates superior rate capability and long-term cycling stability compared to the MrGO/Sb_2O_3 electrode. As shown in Fig. 7a, when the current density increases from 100 mA g^{-1} to 20 000 mA g^{-1}, the MrGO/Sb_2O_3, bare Sb_2O_3, and MrGO electrodes exhibit a sharp decline in capacity performance. In contrast, the PS-MrGO/$Na_xSb_2O_3$ electrode retains a discharge capacity of over 78.0 mA h g^{-1}, even under high current density conditions of 20 000 mA g^{-1}, indicating stable capacity performance at elevated current densities. Furthermore, after the current density is recovered to 100 mA g^{-1} at the 31st cycle, the PS-MrGO/$Na_xSb_2O_3$ electrode sustains a discharge capacity of 386.2 mA h g^{-1} at the 300th cycle. In comparison, the bare Sb_2O_3 electrode loses most of its capacity performance. The comparison of charge/discharge capacities and capacity retention rates over the initial 60 cycles for PS-MrGO/$Na_xSb_2O_3$, MrGO/Sb_2O_3, Sb_2O_3, and MrGO electrodes presented in Fig. 7a is shown in Fig. S20.†

The Ragone plot in Fig. S21† illustrates the energy density (W h kg^{-1}) and power density (W kg^{-1}) of PS-MrGO/$Na_xSb_2O_3$ and MrGO/Sb_2O_3 electrodes in SIBs. The PS-MrGO/$Na_xSb_2O_3$ electrode exhibited superior energy density compared to the MrGO/Sb_2O_3 electrode under various power density conditions.

Fig. 7b illustrates the long-term cycling performance of the electrodes at a high current density of 1200 mA g^{-1}. Due to the formation of an inorganic SEI layer and the amorphization of Sb_2O_3 through pre-sodiation, the PS-MrGO/$Na_xSb_2O_3$ electrode exhibits superior long-term cycling stability compared to the MrGO/Sb_2O_3, bare Sb_2O_3, and MrGO electrodes. After 3000 cycles, the PS-MrGO/$Na_xSb_2O_3$ electrode retains a reversible capacity of 313.5 mA h g^{-1}, demonstrating excellent durability. Peukert's constant in Fig. 7c, an indicator used to assess rate performance, also suggests that the PS-MrGO/$Na_xSb_2O_3$ electrode has a superior rate capability compared to the other electrodes. Additionally, as shown in Fig. 7d–g, the PS-MrGO/$Na_xSb_2O_3$ electrode achieves an ICE of 97.8%. In contrast, the MrGO electrode displays a lower ICE due to the irreversible trapping of Na-ions.

The performance of PS-MrGO/$Na_xSb_2O_3$ and MrGO/Sb_2O_3 electrodes has been compared with the performance metrics of recently reported Sb-based electrodes, as presented in Table S7.†

3.8. Sodium storage kinetics and reaction mechanism

Fig. 8a and b show the CV curves of the PS-MrGO/$Na_xSb_2O_3$ and MrGO/Sb_2O_3 electrodes. Additionally, the CV curves of the MrGO and bare Sb_2O_3 electrodes are presented in Fig. S22.† The CV curves of the MrGO/Sb_2O_3 electrode exhibit reduction peaks at approximately 0.3 V and 0.6 V and oxidation peaks at 0.8 V

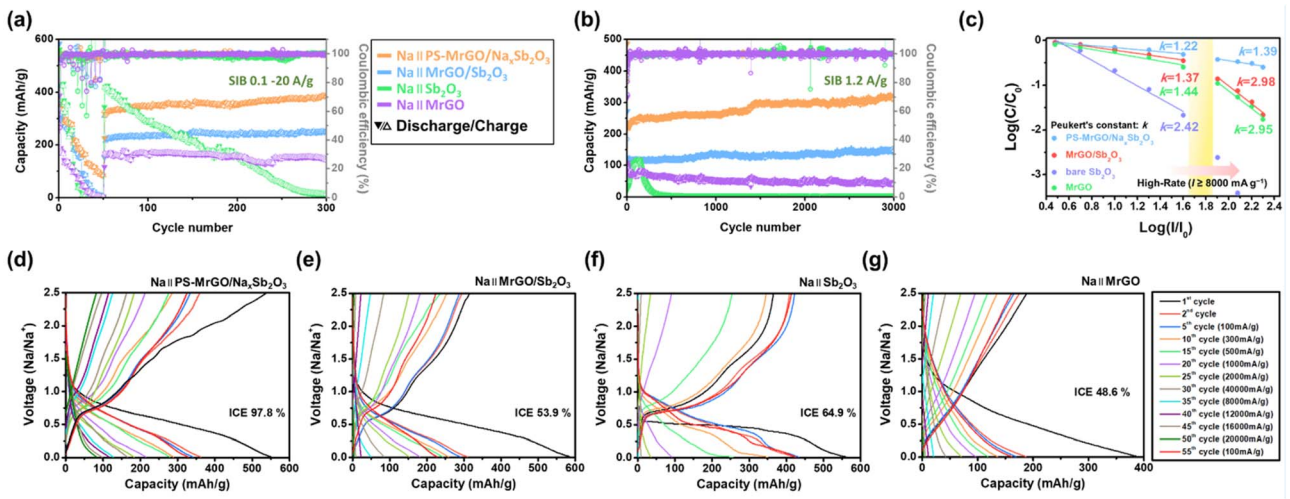

Fig. 7 Sodium storage performance: (a) rate performance of PS-MrGO/$Na_xSb_2O_3$, MrGO/Sb_2O_3, bare Sb_2O_3 and MrGO electrodes at different current densities (100–20 000 mA g^{-1}). (b) Long-term cycling performance at 1200 mA g^{-1}. (c) Peukert's constant for PS-MrGO/$Na_xSb_2O_3$, MrGO/Sb_2O_3, bare Sb_2O_3 and MrGO electrodes. Charge–discharge profiles of (d) PS-MrGO/$Na_xSb_2O_3$, (e) MrGO/Sb_2O_3, (f) bare Sb_2O_3 and (g) MrGO electrodes at different current densities (100–20 000 mA g^{-1}).

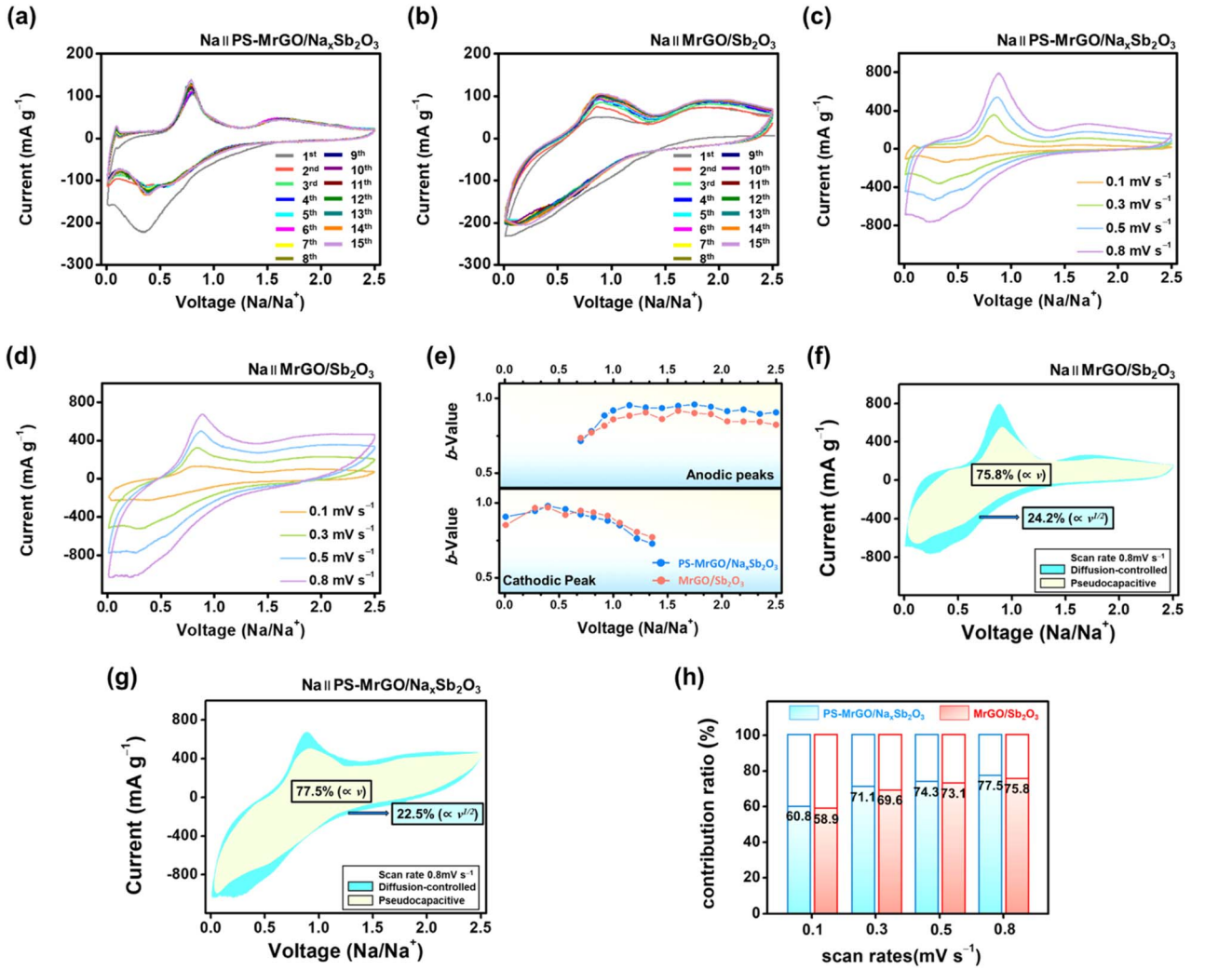

Fig. 8 Sodium storage kinetics analysis: CV profiles of (a) PS-MrGO/$Na_xSb_2O_3$, and (b) MrGO/Sb_2O_3 at a scan rate of 0.1 mV s^{-1}. CV curves of (c) PS-MrGO/$Na_xSb_2O_3$ and (d) MrGO/Sb_2O_3 electrodes at various scan rates (0.1–0.8 mV s^{-1}); (e) comparison of *b*-values at different voltage (0.01–2.5 V); separation of the pseudocapacitive and diffusion-controlled charge storage processes at the (f) PS-MrGO/$Na_xSb_2O_3$ and (g) MrGO/Sb_2O_3 electrodes; (h) comparison of the pseudocapacitive contributions.

and 1.8 V. These peaks correspond to the conversion reactions between antimony oxide and sodium ions.[100–102] In contrast, the PS-MrGO/$Na_xSb_2O_3$ electrode does not show distinct reduction peaks during the first cycle and displays broader peaks compared to the MrGO/Sb_2O_3 electrode. Furthermore, the CV curve exhibits a nearly rectangular shape, which suggests an increased pseudocapacitive behaviour in the electrode.

To further analyze the ion storage behaviour in detail, CV curves were measured at various scan rates (0.1–0.8 mV s^{-1}) (Fig. 8c and d). PS-MrGO/$Na_xSb_2O_3$ and MrGO/Sb_2O_3 electrodes exhibited a gradual shift in redox peak positions with increasing scan rates, along with a linear increase in current density. The peak position shifts were notably more pronounced in the MrGO/Sb_2O_3 electrode than in the PS-MrGO/$Na_xSb_2O_3$ electrode. This observation suggests that the charge storage mechanism in the MrGO/Sb_2O_3 electrode relies more heavily on diffusion-controlled processes. In contrast, the PS-MrGO/$Na_xSb_2O_3$ electrode displayed relatively stable peak shifts, indicating that surface-based pseudocapacitive processes more significantly influence the charge storage mechanism. Additionally, the PS-MrGO/$Na_xSb_2O_3$ electrode demonstrated a *b*-value of approximately 0.94–0.77, confirming that its charge storage mechanism is predominantly governed by pseudocapacitive reactions (Fig. 8e). These findings clearly indicate that the PS-MrGO/$Na_xSb_2O_3$ electrode possesses superior reaction kinetics and enhanced ion diffusion rates on the electrode surface compared to the MrGO/Sb_2O_3 electrode.

In Fig. 8f, the MrGO/Sb_2O_3 electrode exhibits a pseudocapacitive contribution of approximately 75.8% at a scan rate of 0.8 mV s^{-1}. In contrast, the pseudocapacitive contribution of the PS-MrGO/$Na_xSb_2O_3$ electrode remains 77.5%, as shown in Fig. 8g. Furthermore, Fig. 8h illustrates that the PS-MrGO/$Na_xSb_2O_3$ electrode consistently demonstrates higher pseudocapacitive contributions across all scan rates (0.1–0.8 mV s^{-1}) compared to the MrGO/Sb_2O_3 electrode. These findings highlight the enhanced electrochemical reactivity at the electrode

surface, attributed to the robust composite structure formed by integrating PS-MrGO and $Na_xSb_2O_3$. Additionally, the stabilization of the SEI plays a role in maintaining the high pseudocapacitive behaviour of the PS-MrGO/$Na_xSb_2O_3$ electrode.

Fig. 9a–c show the Nyquist plots of the PS-MrGO/$Na_xSb_2O_3$, MrGO/Sb_2O_3, and MrGO electrodes. The EIS analysis results for the bare Sb_2O_3 electrode are presented in Fig. S23.† The PS-MrGO/$Na_xSb_2O_3$ and MrGO/Sb_2O_3 electrodes exhibit lower high-frequency resistance (film resistance) and mid-frequency charge transfer resistance compared to the MrGO and bare Sb_2O_3 electrodes during both the initial charge/discharge cycle and the 100th cycle.

According to the DRT analysis, the PS-MrGO/$Na_xSb_2O_3$ electrode exhibits relatively low resistance across all frequency ranges (Fig. 9d–f). In particular, this electrode shows a minimal resistance increase due to the formation of the SEI layer. These results indicate that the PS-MrGO/$Na_xSb_2O_3$ electrode possesses high electrical conductivity and stable interfacial properties, with low kinetic barriers for electrode reactions. In contrast, the MrGO and bare Sb_2O_3 electrodes exhibit significant resistance increases attributed to SEI layer formation, as revealed by the DRT analysis (Fig. S23†). This suggests that these electrodes have non-uniform electrochemical active sites and suffer from substantial degradation in reactivity after cycling. Compared to the PS-MrGO/$Na_xSb_2O_3$ electrode, the increased SEI resistance observed in the bare Sb_2O_3 electrodes reflects structural deterioration. These factors act as major limitations to the long-term performance stability of these electrodes. As shown in Fig. 9g and h, ECM fitting was performed to quantitatively separate the electrochemical resistance components of each electrode. The impedance parameters obtained from the EIS data fitting are provided in Table S8.† The PS-MrGO/$Na_xSb_2O_3$ electrode exhibited the lowest charge transfer resistance and SEI resistance, which can be attributed to the formation of a stable and highly conductive interfacial structure facilitated by chemical pre-sodiation. Furthermore, the PS-MrGO/

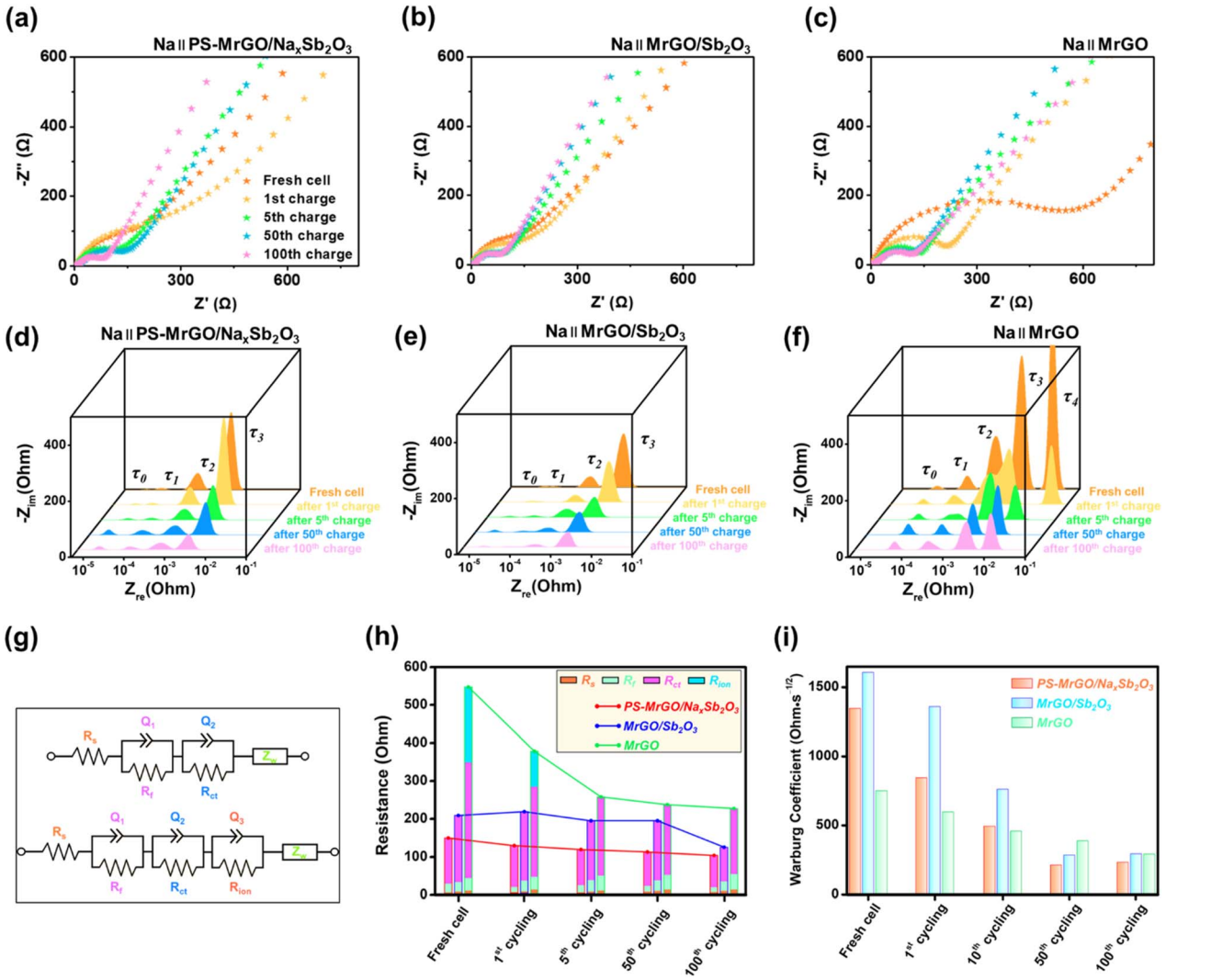

Fig. 9 Electrochemical impedance spectroscopy analysis in SIBs: Nyquist plot of the (a) PS-MrGO/$Na_xSb_2O_3$, (b) MrGO/Sb_2O_3 and (c) MrGO electrodes measured up to the 100th cycle. DRT plot of the (d) PS-MrGO/$Na_xSb_2O_3$, (e) MrGO/Sb_2O_3 and (f) MrGO electrodes. (g) ECM for fitting EIS data (the impedance parameters are provided in Table S8†). (h) Comparison of the parameters from the ECM fits and (i) Warburg coefficients.

$Na_xSb_2O_3$ electrode exhibited a low Warburg coefficient even after 100 cycles, indicating a reduction in diffusion resistance during cycling (Fig. 9i).

In conclusion, the PS-MrGO/$Na_xSb_2O_3$ electrode demonstrated excellent capacity performance and long-term cycling stability in SIBs, achieved through the stabilization of the SEI layer, low charge transfer resistance, and enhanced ionic conductivity.

4 Conclusions

In this study, PL(S)-MrGO/Li(Na)$_x$$Sb_2O_3$ electrodes, exhibiting excellent performance in LIBs and SIBs, were developed through a simple and efficient synthesis method involving ultrasonication, microwave processing, and chemical pre-lithiation/sodiation. The PL(S)-MrGO/Li(Na)$_x$$Sb_2O_3$ electrode achieved an ICE close to 100%, with the formation of an inorganic SEI layer and amorphization of Sb_2O_3 contributing to the suppression of irreversible Li/Na-ion trapping. These features minimized irreversible reactions during charge/discharge cycles, enhancing long-term cycling stability and electrical conductivity. Notably, the PL(S)-MrGO/Li(Na)$_x$$Sb_2O_3$ electrode demonstrated superior long-term cycling stability and high-rate performance compared to the MrGO/Sb_2O_3, bare Sb_2O_3, and MrGO electrodes. This approach presents a promising solution to address the initial capacity loss and low ICE issues frequently observed in conventional reduced graphene oxide and antimony oxide-based electrodes.

Data availability

The data supporting this article have been included as part of the ESI.†

Author contributions

Minseop Lee: conceptualization, methodology, synthesis, characterization, writing – original draft. Gi-Chan Kim: investigation, synthesis, characterization, Seung-Min Paek: methodology, supervision, validation, funding acquisition, writing – review & editing.

Conflicts of interest

The authors declare no competing financial interests.

Acknowledgements

This study was supported by grants from the Basic Science Research Program (RS-2024-00345599).

References

1 P. Simon and Y. Gogotsi, *Nat. Mater.*, 2020, **19**, 1151–1163.
2 T. Cao, C. Zhu, X. Wang, Z. Ji, H. Liang, J. Shi, W. Tian, J. Chen, J. Wu and H. Wang, *Sustain. Energy Fuels*, 2024, **8**, 4790–4798.
3 F. Huang, P. Xu, G. Fang and S. Liang, *Adv. Mater.*, 2024, **36**, 2405310.
4 P. Xu, F. Huang, Y. Sun, Y. Lei, X. Cao, S. Liang and G. Fang, *Adv. Funct. Mater.*, 2024, **34**, 2406080.
5 J. Khan, A. Ahmed, M. I. Saleem and A. A. Al-Kahtani, *Sustain. Energy Fuels*, 2024, **8**, 4355–4364.
6 M. Lee, J. Xie, J.-M. Oh and S.-M. Paek, *Chem. Eng. J.*, 2025, **506**, 159671.
7 P. Kulkarni, H. Jung, D. Ghosh, M. Jalalah, M. Alsaiari, F. A. Harraz and R. G. Balakrishna, *J. Energy Chem.*, 2023, **76**, 479–494.
8 L. Jin, C. Shen, Q. Wu, A. Shellikeri, J. Zheng, C. Zhang and J. P. Zheng, *Adv. Sci.*, 2021, **8**, 2005031.
9 Y. Wang, J. Lu, W. Dai, X. Cheng, J. Zuo, H. Lei, W. Liu and Z. Fu, *Adv. Funct. Mater.*, 2024, **34**, 2403841.
10 J. S. Ko, B. Tan, M. W. Logan, S. A. Langevin and K. Gerasopoulos, *J. Mater. Chem. A*, 2024, **12**, 14354–14359.
11 T. Panneerselvam, R. Murugan and O. V. Sreejith, *Sustain. Energy Fuels*, 2024, **8**, 1704–1711.
12 S. Lin, H. Zhang, C. Shu, W. Hua, X. Wang, Y. Zhao, J. Luo, Z. Tang, Y. Wu and W. Tang, *Adv. Funct. Mater.*, 2024, **34**, 2409628.
13 Q. Liu, J. Chen, D. Du, S. Zhang, C. Zhu, Z. Zhang, C. Wang, L. Yin and R. Wang, *J. Mater. Chem. A*, 2023, **11**, 17491–17502.
14 C. Guo, B. Zhang, M. Xiao, M. Hao, L. Zhao, X. Zhang, H. Zhang and R. Wang, *Sustain. Energy Fuels*, 2024, **8**, 837–842.
15 Z. Lin, H. Zhang, C. Yang, Z. Liu, D. Wen, X. Peng, S. Li and X. Wu, *Sustain. Energy Fuels*, 2024, **8**, 934–941.
16 Z. Li, M. Du, X. Guo, D. Zhang, Q. Wang, H. Sun, B. Wang and Y. A. Wu, *Chem. Eng. J.*, 2023, **473**, 145294.
17 M. Yasoubi, A. Habibi, S. Hoornam, Z. Sanaee and S. Mohajerzadeh, *Sustain. Energy Fuels*, 2024, **8**, 3419–3437.
18 M. Lee, S. Park, B. Bae, Y. K. Jeong, J.-M. Oh, J. K. Park and S.-M. Paek, *Chem. Eng. J.*, 2023, **477**, 147072.
19 R. Wang, L. Wang, R. Liu, X. Li, Y. Wu and F. Ran, *ACS Nano*, 2024, **18**, 2611–2648.
20 R. Mo, F. Li, X. Tan, P. Xu, R. Tao, G. Shen, X. Lu, F. Liu, L. Shen, B. Xu, Q. Xiao, X. Wang, C. Wang, J. Li, G. Wang and Y. Lu, *Nat. Commun.*, 2019, **10**, 1–10.
21 C. S. Bongu, S. Tasleem, M. R. Krishnan and E. H. Alsharaeh, *Sustain. Energy Fuels*, 2024, **8**, 4039–4070.
22 C.-Y. Wang, T. Liu, X.-G. Yang, S. Ge, N. V. Stanley, E. S. Rountree, Y. Leng and B. D. McCarthy, *Nature*, 2022, **611**, 485–490.
23 M. Lee and S.-M. Paek, *Nanomaterials*, 2022, **12**, 1507.
24 M. Lee, M.-S. Kim, J.-M. Oh, J. K. Park and S.-M. Paek, *ACS Nano*, 2023, **17**, 3019–3036.
25 C. Wang, S. Xue, X. Lei, J. Wen, X. Pan, F. Zhang, C. Zou and Y. Tang, *Chem. Eng. J.*, 2023, **470**, 144043.
26 D. Zhao, Z. Zhang, J. Ren, Y. Xu, X. Xu, J. Zhou, F. Gao, H. Tang, S. Liu, Z. Wang, D. Wang, Y. Wu, X. Liu and Y. Zhang, *Chem. Eng. J.*, 2023, **451**, 138882.
27 J. Rehman, J. Gao, T. Yu, A. El-marghany and G. Yang, *J. Mater. Chem. A*, 2024, **12**, 6703–6711.

28 S. Liang, Y.-J. Cheng, J. Zhu, Y. Xia and P. Müller-Buschbaum, *Small Methods*, 2020, **4**, 2000218.
29 S. Sarkar and S. C. Peter, *J. Mater. Chem. A*, 2021, **9**, 5164–5196.
30 W. T. Jing, C. C. Yang and Q. Jiang, *J. Mater. Chem. A*, 2020, **8**, 2913–2933.
31 L. Feng, J. Chen, Y. Li, S. Zhou, R. A. Soomro, P. Zhang and B. Xu, *Chem. Eng. J.*, 2024, **489**, 151396.
32 X. Shi, W. Liu, H. Xue, B. Chen, C. Wang, L. Sun, L. Chang, Y. Cheng and L. Wang, *J. Power Sources*, 2021, **506**, 230074.
33 A. Xu, C. Huang, G. Li, K. Zou, H. Sun, L. Fu, J. Ju, Y. Song, S. Wu, Z. Xu and Y. Yan, *J. Mater. Chem. A*, 2021, **9**, 12169–12178.
34 H. Bryngelsson, J. Eskhult, L. Nyholm, M. Herranen, O. Alm and K. Edström, *Chem. Mater.*, 2007, **19**, 1170–1180.
35 S. Kim, S. Qu, R. Zhang and P. V. Braun, *Small*, 2019, **15**, 1900258.
36 J. Zheng, Y. Yang, X. Fan, G. Ji, X. Ji, H. Wang, S. Hou, M. R. Zachariah and C. Wang, *Energy Environ. Sci.*, 2019, **12**, 615–623.
37 J. Song, P. Yan, L. Luo, X. Qi, X. Rong, J. Zheng, B. Xiao, S. Feng, C. Wang, Y.-S. Hu, Y. Lin, V. L. Sprenkle and X. Li, *Nano Energy*, 2017, **40**, 504–511.
38 Y. Li, Z. Song, T. Sun, Y. Shen, X. Lv, D. Xu and H.-G. Wang, *Int. J. Hydrogen Energy*, 2021, **46**, 26308–26317.
39 Z. Yi, Q. Han, P. Zan, Y. Wu, Y. Cheng and L. Wang, *J. Power Sources*, 2016, **331**, 16–21.
40 B. Jin, K. Zhang, G. Gao, Q. Zhao, X. Jiang, D. Cui, K. Chen, X. Lin, L. Liu, R. Yan, B. Yang and Y. Yao, *Chem. Eng. J.*, 2024, **493**, 152542.
41 R. Yi, S. Hu, L. Zheng, Y. Li, W. Luo, H. Zhang, J. Ge, Y. Shen and L. Chen, *Chem. Eng. J.*, 2024, **500**, 157201.
42 X. Li, X. Sun, X. Hu, F. Fan, S. Cai, C. Zheng and G. D. Stucky, *Nano Energy*, 2020, **77**, 105143.
43 D. Liu, Y. Qiu, Y. Du, J. Yang, X. Jing, X. Peng, Q. Song and F. Xu, *J. Mater. Chem. A*, 2024, **12**, 16695–16703.
44 H. He, D. Sun, Y. Tang, H. Wang and M. Shao, *Energy Storage Mater.*, 2019, **23**, 233–251.
45 L. Sun, Y. Liu, J. Wu, R. Shao, R. Jiang, Z. Tie and Z. Jin, *Small*, 2022, **18**, 2102894.
46 M. Liu, F. Wu, Y. Gong, Y. Li, Y. Li, X. Feng, Q. Li, C. Wu and Y. Bai, *Adv. Mater.*, 2023, **35**, 2300002.
47 R. Shao, Z. Sun, L. Wang, J. Pan, L. Yi, Y. Zhang, J. Han, Z. Yao, J. Li, Z. Wen, S. Chen, S.-L. Chou, D.-L. Peng and Q. Zhang, *Angew. Chem.*, 2024, **136**, 2320183.
48 J. Yang, J. Li, T. Wang, P. H. L. Notten, H. Ma, Z. Liu, C. Wang and G. Wang, *Chem. Eng. J.*, 2021, **407**, 127169.
49 H. Li, K. Qian, X. Qin, D. Liu, R. Shi, A. Ran, C. Han, Y.-B. He, F. Kang and B. Li, *J. Power Sources*, 2018, **385**, 114–121.
50 W. S. Hummers Jr and R. E. Offeman, *J. Am. Chem. Soc.*, 1958, **80**, 1339.
51 T. H. Wan, M. Saccoccio, C. Chen and F. Ciucci, *Electrochim. Acta*, 2015, **184**, 483–499.
52 W. Zhang, H. Xu, F. Xie, X. Ma, B. Niu, M. Chen, H. Zhang, Y. Zhang and D. Long, *Nat. Commun.*, 2022, **13**, 1–10.
53 J. Jang, I. Kang, J. Choi, H. Jeong, K.-W. Yi, J. Hong and M. Lee, *Angew. Chem.*, 2020, **59**, 14473–14480.
54 G. Wang, F. Li, D. Liu, D. Zheng, Y. Luo, D. Qu, T. Ding and D. Qu, *ACS Appl. Mater. Interfaces*, 2019, **11**, 8699–8703.
55 J. Peng, D. Wu, P. Lu, Z. Wang, Y. Du, Y. Wu, Y. Wu, W. Yan, J. Wang, H. Li, L. Chen and F. Wu, *Energy Storage Mater.*, 2023, **54**, 430–439.
56 Y. Kim, J. Jung, H. Yu, G.-T. Kim, D. Jeong, D. Bresser, S. J. Kang, Y. Kim and S. Passerini, *Adv. Funct. Mater.*, 2020, **30**, 2001249.
57 X. Liu, Y. Tan, T. Liu, W. Wang, C. Li, J. Lu and Y. Sun, *Adv. Funct. Mater.*, 2019, **29**, 1903795.
58 K. Zou, W. Deng, P. Cai, X. Deng, B. Wang, C. Liu, J. Li, H. Hou, G. Zou and X. Ji, *Adv. Funct. Mater.*, 2021, **31**, 2005581.
59 G. Zheng, Q. Lin, J. Ma, J. Zhang, Y.-B. He, X. Tang, F. Kang, W. Lv and Q.-H. Yang, *InfoMat*, 2021, **3**, 1445–1454.
60 M. Liu, J. Zhang, S. Guo, B. Wang, Y. Shen, X. Ai, H. Yang and J. Qian, *ACS Appl. Mater. Interfaces*, 2020, **12**, 17620–17627.
61 M. Liu, Z. Yang, Y. Shen, S. Guo, J. Zhang, X. Ai, H. Yang and J. Qian, *J. Mater. Chem. A*, 2021, **9**, 5639–5647.
62 R. Mei, X. Song, Y. Hu, Y. Yang and J. Zhang, *Electrochim. Acta*, 2015, **153**, 540–545.
63 D. Jiao, Z. Xie, Q. Wan and M. Qu, *J. Energy Chem.*, 2019, **37**, 73–81.
64 S. Wu, G. Fu, W. Lv, J. Wei, W. Chen, H. Yi, M. Gu, X. Bai, L. Zhu, C. Tan, Y. Liang, G. Zhu, J. He, X. Wang, K. H. L. Zhang, J. Xiong and W. He, *Small*, 2018, **14**, 1702667.
65 X. Dong, L. Li, C. Zhao, H.-K. Liu and Z. Guo, *J. Mater. Chem. A*, 2014, **2**, 9844–9850.
66 W.-J. Lee, H.-R. Jang, M.-J. Kim, H.-M. Kim, J.-M. Oh and S.-M. Paek, *J. Alloys Compd.*, 2019, **778**, 382–390.
67 G. Huang, P. Song, L. Liu, D. Han, C. Ge, R. Li and Q. Guo, *Carbon*, 2016, **98**, 689–701.
68 K. P. Lakshmi, R. Deivanayagam and M. M. Shaijumon, *J. Alloys Compd.*, 2021, **857**, 158267.
69 N. Li, Y. Xia, Z. Mao, L. Wang, Y. Guan and A. Zheng, *Polym. Degrad. Stab.*, 2012, **97**, 1737–1744.
70 X. Yang, Y. Zhu, D. Wu, M. Li, Y. He, L. Huang and M. Gu, *Adv. Funct. Mater.*, 2022, **32**, 2111391.
71 L. Zhang, Y. Song, Y. Hu, H. Ruan, J. Bai, S. Li, Y. Liu and S. Guo, *J. Alloys Compd.*, 2022, **890**, 161913.
72 X. Zhou, Z. Zhang, X. Lu, X. Lv, G. Ma, Q. Wang and Z. Lei, *ACS Appl. Mater. Interfaces*, 2017, **9**, 34927–34936.
73 K. Pfeifer, M. F. Greenstein, D. Aurbach, X. Luo, H. Ehrenberg and S. Dsoke, *Chemelectrochem*, 2020, **7**, 3487–3495.
74 O. A. Jaramillo-Quintero, R. V. Barrera-Peralta, A. Baron-Jaimes, R. A. Miranda-Gamboa and M. E. Rincon, *RSC Adv.*, 2021, **11**, 31566–31571.
75 Z. Han, J. Zheng, F. Kong, S. Tao and B. Qian, *Nano Sel.*, 2021, **2**, 425–432.
76 M. B. Costa, F. W. S. Lucas, M. Medina and L. H. Mascaro, *ACS Appl. Energy Mater.*, 2020, **3**, 9799–9808.

77 F. Zhang, W. Zhang, J. A. Yuwono, D. Wexler, Y. Fan, J. Zou, G. Liang, L. Sun and Z. Guo, *Nat. Commun.*, 2024, **15**, 1–11.
78 B. Zhao, J. Li, M. Guillaume, J. Dendooven and C. Detavernier, *J. Energy Chem.*, 2022, **66**, 295–305.
79 S. Malmgren, K. Ciosek, R. Lindblad, S. Plogmaker, J. Kühn, H. Rensmo, K. Edström and M. Hahlin, *Electrochim. Acta*, 2013, **105**, 83–91.
80 J. P. Tonks, M. O. King, E. C. Galloway and J. F. Watts, *J. Nucl. Mater.*, 2017, **484**, 228–235.
81 N. Hornsveld, B. Put, W. M. M. Kessels, P. M. Vereecken and M. Creatore, *RSC Adv.*, 2017, **7**, 41359–41368.
82 M. L. Kalapsazova, E. N. Zhecheva, G. T. Tyuliev, D. D. Nihtianova, L. Mihaylov and R. K. Stoyanova, *J. Phys. Chem. C*, 2017, **121**, 5931–5940.
83 C. Hou, Z. Yue, H. Sun, L. Zhai, H. Xie, H. Tian, Y. Qu, X. Wang and J. Hou, *J. Mater. Sci.: Mater. Electron.*, 2024, **35**, 956.
84 B. Qin, A. Schiele, Z. Jusys, A. Mariani, T. Diemant, X. Liu, T. Brezesinski, R. J. Behm, A. Varzi and S. Passerini, *ACS Appl. Mater. Interfaces*, 2020, **12**, 3697–3708.
85 Z. Wang, Y. Cheng, Q. Li, L. Chang and L. Wang, *J. Power Sources*, 2018, **389**, 214–221.
86 Z. Wang, F. Zeng, D. Zhang, X. Wang, W. Yang, Y. Cheng, C. Li and L. Wang, *Electrochim. Acta*, 2021, **395**, 139210.
87 O. A. Jaramillo-Quintero, M. Benítez-Cruz, J. L. García-Ocampo, A. Cano and M. E. Rincón, *J. Alloys Compd.*, 2019, **807**, 151647.
88 V. Augustyn, P. Simon and B. Dunn, *Energy Environ. Sci.*, 2014, **7**, 1597.
89 C. Choi, D. S. Ashby, D. M. Butts, R. H. DeBlock, Q. Wei, J. Lau and B. Dunn, *Nat. Rev. Mater.*, 2019, **5**, 5–19.
90 M. Lee, J.-H. Park and S.-M. Paek, *New J. Chem.*, 2024, **48**, 2381–2388.
91 J.-H. Jang, M. Lee, S. Park, J.-M. Oh, J. K. Park and S.-M. Paek, *J. Mater. Chem. A*, 2023, **11**, 13320–13330.
92 Y. Lu, C.-Z. Zhao, J.-Q. Huang and Q. Zhang, *Joule*, 2022, **6**, 1172–1198.
93 X. Zhou, Z. Pan, X. Han, L. Lu and M. Ouyang, *J. Power Sources*, 2019, **417**, 188–192.
94 Y. Lu, C.-Z. Zhao, R. Zhang, H. Yuan, L.-P. Hou, Z.-H. Fu, X. Chen, J.-Q. Huang and Q. Zhang, *Sci. Adv.*, 2021, **7**, eabi5520.
95 J.-H. Jang, M. Lee, J.-H. Koo and S.-M. Paek, *Int. J. Mol. Sci.*, 2022, **23**, 11766.
96 B. Manikandan, V. Ramar, C. Yap and P. Balaya, *J. Power Sources*, 2017, **361**, 300–309.
97 M.-S. Kim, M. Lee, M.-J. Kim, Y. K. Jeong, J. K. Park and S.-M. Paek, *J. Mater. Chem. A*, 2020, **8**, 17790–17799.
98 M. Lee, M.-S. Kim, J.-M. Oh, J. K. Park and S.-M. Paek, *ChemSusChem*, 2021, **14**, 3244–3256.
99 M. Liang, H. Zhang, B. Chen, X. Meng, J. Zhou, L. Ma, F. He, W. Hu, C. He and N. Zhao, *Adv. Mater.*, 2023, **35**, 2307209.
100 M. Hu, Y. Jiang, W. Sun, H. Wang, C. Jin and M. Yan, *ACS Appl. Mater. Interfaces*, 2014, **6**, 19449–19455.
101 B. Selvaraj, C.-C. Wang, Y.-F. Song, H.-S. Sheu, Y.-F. Liao and N.-L. Wu, *J. Mater. Chem. A*, 2020, **8**, 22620–22625.
102 W. Ma, J. Wang, H. Gao, J. Niu, F. Luo, Z. Peng and Z. Zhang, *Energy Storage Mater.*, 2018, **13**, 247–256.